



Grain boundary stresses in elastic materials

S. El Shawish^{*}, T. Mede

Jožef Stefan Institute, SI-1000, Ljubljana, Slovenia

ARTICLE INFO

Keywords:

Grain boundaries
Microstructures
Stress distributions
Anisotropic elasticity
Perturbation theory
Finite elements

ABSTRACT

A simple analytical model of intergranular normal stresses is proposed for a general elastic polycrystalline material with arbitrary shaped and randomly oriented grains under uniform loading. The model provides algebraic expressions for the local grain-boundary-normal stress and the corresponding uncertainties, as a function of the grain-boundary type, its inclination with respect to the direction of external loading and material-elasticity parameters. The knowledge of intergranular normal stresses is a necessary prerequisite in any local damage modeling approach, *e.g.*, to predict the probability for intergranular stress-corrosion cracking or fatigue-crack initiation in structural materials.

The model is derived in a perturbative manner, starting with the exact solution of a simple setup and later successively refining it to account for higher order complexities of realistic polycrystalline materials. In the simplest scenario, a bicrystal model is embedded in an isotropic elastic medium and solved for uniaxial loading conditions, assuming 1D Reuss and Voigt approximations on different length scales. In the final iteration, the grain boundary becomes a part of a 3D structure consisting of five 1D chains with arbitrary number of grains and surrounded by an anisotropic elastic medium. Constitutive equations can be solved for arbitrary uniform loading, for any grain-boundary type and choice of elastic polycrystalline material. At each iteration, the algebraic expressions for the local grain-boundary-normal stress, along with the corresponding statistical distributions, are derived and their accuracy systematically verified and validated against the finite element simulation results of different Voronoi microstructures.

1. Introduction

Predicting damage initiation and its progression in structural materials relies heavily on the knowledge of local mechanical stresses present in the material. For particular aging processes, the material damage is initiated at the grain boundaries (GBs), where intergranular microcracks form. With time, these microcracks may grow along the GBs and combine into larger macroscopic cracks, which can eventually compromise the structural integrity of the entire component under load. Since microcracks are invisible to non-destructive inspection techniques, the detection instruments can only reveal the existence of macroscopic cracks, which roughly appear in the final 10% of the component's lifetime. Having accurate models for predicting the component's susceptibility to microcracking in its earlier stages is therefore of uttermost importance in many different applications, as this could reduce the costs needed for frequent inspections and replacements.

InterGranular Stress-Corrosion Cracking (IGSCC) is one of the most significant ageing-degradation mechanisms. It corresponds to the initiation and propagation of microcracks along the GBs and is common in

alloys, that are otherwise typically corrosion-resistant (austenitic stainless steels (Nishioka et al., 2008; Le Millier et al., 2013; Stephenson and Was, 2014; Gupta et al., 2016; Fujii et al., 2019), zirconium alloys (Cox, 1970, 1990), nickel based alloys (Van Rooyen, 1975; Shen and Shewmon, 1990; Panter et al., 2006; IAEA, 2011), high strength aluminum alloys (Speidel, 1975; Burleigh, 1991) and ferritic steels (Wang and Atrens, 1996; Arafin and Szpunar, 2009)). The IGSCC is a multi-level process that includes electro-chemical, micro-mechanical and thermo-mechanical mechanisms. The activation of these mechanisms depends on material properties, corrosive environment and local stress state. It is believed that GB stresses are the driving force of intergranular cracking, therefore they need to be accurately determined, in order to make quantitative predictions about IGSCC initiation.

Various approaches to IGSCC-initiation modeling are being considered. One such approach is to treat IGSCC phenomenon on a local GB scale, where GB-normal stresses σ_{nn} can be studied separately (decoupled) from the environmental effects that degrade the GB strength σ_c ; $IGSCC \approx \mathcal{F}(\sigma_{nn}) \cdot \mathcal{F}(\sigma_c)$. A GB-normal stress σ_{nn} is defined here as a component of local stress tensor along the GB-normal direction, *i.e.*,

^{*} Corresponding author.

E-mail addresses: samir.elshawish@ijs.si (S. El Shawish), timon.mede@ijs.si (T. Mede).

¹ In the terminology of fracture mechanics, σ_{nn} corresponds to the opening-mode stress (Mode I).

perpendicular to the GB plane.¹ Hence, a single stress-based criterion for a local IGSCC initiation can be assumed on every GB: IGSCC gets initiated wherever $\sigma_{nn} > \sigma_c$, with both these quantities being local in a sense, that they in principle depend on the position of the GB within the aggregate.

The introduced local criterion can be used to evaluate the probability, that a randomly selected GB on a component's surface, where it is in contact with the corrosive environment, is overloaded (or soon-to-be cracked). This probability can be estimated by calculating a fraction η of GBs with $\sigma_{nn} > \sigma_c$ as $\eta = \int_{\sigma_c}^{\infty} \text{PDF}(\sigma_{nn}) d\sigma_{nn}$, for the assumed probability-density function $\text{PDF}(\sigma_{nn})$. If a fraction of overloaded GBs exceeds a threshold value, $\eta > \eta_f$, a specimen-sized crack may develop, possibly resulting in a catastrophic failure of the component. This approach, based on the accurate knowledge of GB-normal-stress distribution, seems feasible when a GB strength σ_c is known and approximately constant within the examined surface section. Unfortunately, this is not the case in real materials.

Measurements have shown that different GBs show different IGSCC sensitivities (Rahimi and Marrow, 2011; Fujii et al., 2019; Rahimi et al., 2009; Liu et al., 2019), implying that GB strength σ_c depends not only on the material and environmental properties but also strongly on a GB type; $\sigma_c = \mathcal{F}(\text{GB type, material, environment})$. Here, a GB type denotes a GB microstructure (inter-atomic arrangements in the vicinity of the GB), which affects the GB energy and, eventually, its strength σ_c . In the continuum limit, five parameters are needed to define a GB neighborhood: four parameters are required to specify a GB plane in crystallographic systems of the two adjacent grains and one parameter defines a twist rotation between the associated crystal lattices about the plane normal. In principle, the term "GB type" thus refers to GBs with the same GB strength. Sometimes it is convenient to specify a GB type by less than five parameters (e.g., when the values of skipped parameters do not affect the σ_{nn} distribution). For instance, in the $[abc]$ - $[def]$ GB type, with a GB-plane normal along the $[abc]$ direction in one grain and $[def]$ direction in the other grain, the twist angle can be assumed random (and thus remains unspecified).

In addition to σ_c being a function of GB type, also the distributions of GB-normal stresses should be evaluated for different GB types in order to later perform a meaningful calculation of fraction η . Hence, $\text{PDF}(\sigma_{nn}) = \mathcal{F}(\text{GB type, applied stress, material})$. Since exact general solutions for both the local σ_{nn} and statistical $\text{PDF}(\sigma_{nn})$ are too complex to be derived analytically, researchers have restricted themselves to numerical simulations limited to few selected materials and specific (usually uniaxial) loading conditions.

Crystal-plasticity finite element (FE) simulations (Diard et al., 2002, 2005; Kanjarla et al., 2010; Gonzalez et al., 2014; Hure et al., 2016; El Shawish and Hure, 2018) and crystal-plasticity fast Fourier transform simulations (Lebensohn et al., 2012; Liang et al., 2021) have been used to obtain intergranular stresses on random GBs in either synthetic or realistic polycrystalline aggregates, providing valuable information for IGSCC initiation in those specific cases.² In particular, the fluctuations of intergranular normal stresses (the widths of $\text{PDF}(\sigma_{nn})$) have been found to depend primarily on the elasto-plastic anisotropy of the grains with either cubic (Gonzalez et al., 2014; Hure et al., 2016; El Shawish

² As an interesting alternative to FE simulations one can consider the Boundary Element Method, which is an efficient approach to a wide range of fracture problems (IGSCC, low- and high-cycle fatigue, micro-cracking, etc.) which require only the knowledge of boundary responses without resolving the whole system. Its framework is particularly well suited for modeling solid objects in contact, such as the grains in polycrystalline materials, and to evaluate stresses and displacements at the GBs with high accuracy while keeping the computational time low because stress-strain fields within the grains are not being calculated. The method has been successfully applied to the case of 2D (Sfantos and Aliabadi, 2007) and 3D polycrystals (Benedetti and Aliabadi, 2013b,a).

and Hure, 2018) or hexagonal lattice symmetries (El Shawish and Hure, 2018).

Although the computationally demanding simulations can provide accurate results, such an approach deems impractical for a general case and provides little insights into involved physics. Thus, efforts have been made to identify most influential parameters affecting the GB-normal stresses on any single GB type (West and Was, 2011; El Shawish et al., 2021). In the elastic regime of grains with cubic lattice symmetry, Zener elastic anisotropy index A (Zener, 1948) and effective GB stiffness E_{12} , measuring the average stiffness of GB neighborhood along the GB-normal direction, have been identified and demonstrated to be sufficient for quantifying normal-stress fluctuations on any GB type in a given material under uniaxial external loading (El Shawish et al., 2021). The empirical relation (still lacking a satisfactory explanation) has been established for the standard deviation of σ_{nn} distribution evaluated on $[abc]$ - $[def]$ GBs, which is a function of A and E_{12} . On the contrary, the mean value of the same σ_{nn} distribution has been shown to be independent of the chosen material and/or the GB type on which it is calculated.

To account for elastic-perfectly plastic grains at applied tensile yield stress, a simple Schmid-Modified Grain-Boundary-Stress model has been proposed (West and Was, 2011) to investigate the initiation of an intergranular crack, based on a normal stress acting at GB. The model considers combined effects of GB-plane orientation and grain orientations through their Schmid factors. It has been pointed out, that intergranular cracks occur most likely at highly stressed GBs. In other similar studies (Stratulat et al., 2014; Zhang et al., 2019; Fujii et al., 2019), the same model has been used to discuss crack initiation in austenitic stainless steel, concluding that initiation sites coincide with the most highly stressed GBs.

Building upon partial results, limited to either specific loading conditions (West and Was, 2011; El Shawish et al., 2021) and/or specific grain-lattice symmetries (El Shawish et al., 2021), the goal of this study is to develop a model of GB-normal stresses, that would provide analytic or semi-analytic expressions for σ_{nn} , with accurate statistical measure $\text{PDF}(\sigma_{nn})$, depending on a general GB type, general applied stress and general elastic polycrystalline material. Once the knowledge of GB strength σ_c becomes available, the resulting expressions will be directly useful in the mechanistic modeling of GB-damage initiation (such as IGSCC³) and should therefore become a quick and reliable tool to all the experts dealing with local damage modeling and characterization.

The paper is structured as follows: in Section 2 typical material and GB-type effects on GB-normal stresses are introduced. In Section 3 the perturbative framework for predicting GB-normal stresses is developed, providing analytical and semi-analytical models along with their solutions. In Section 4 the upgraded models are verified with FE-simulation results. Practical implications are discussed in Section 5 and in Section 6 some concluding remarks are given. All technical details are deferred to the set of Appendices.

2. Material and grain boundary type effects on intergranular normal stresses

The anisotropic elasticity of crystals is governed by the generalized Hooke's law, $\sigma_{ij} = C_{ijkl} \epsilon_{kl}$, where C_{ijkl} is a 3D fourth-order stiffness tensor. Depending on the symmetry of the underlying grain lattice, C_{ijkl} can be expressed in terms of two (isotropic), three (cubic), or more (up to 21 for triclinic) independent elastic parameters. All grains in a polycrystalline aggregate are assigned the same elastic material

³ Since material and mechanical aspects of IGSCC are decoupled from the environmental factors hidden in the GB strength, this study may also be relevant for other degradation mechanisms, where GB-normal stresses are the driving force for crack initiation, such as fatigue.

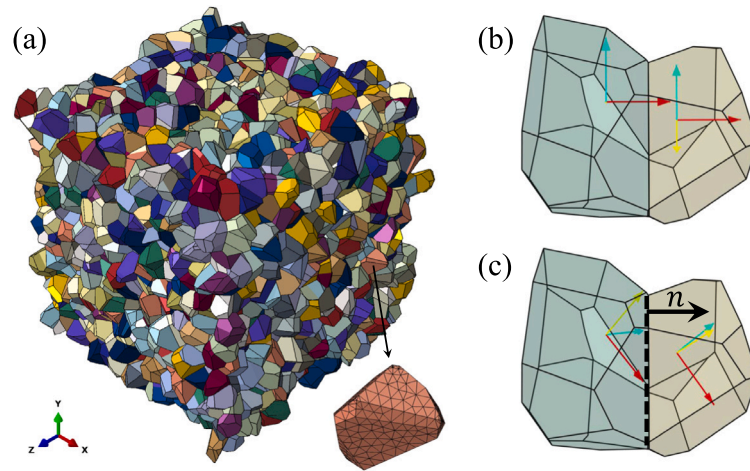


Fig. 1. (a) 3D periodic Voronoi aggregate with 4000 grains used in this study. Different grains are denoted by different colors. Finite element mesh is shown for one selected grain. Visualization of two different GBs with fixed GB plane (with normal n) but different crystallographic orientations: (b) [001]-[001]-30° GB and (c) [111]-[111]-30° GB.

properties, but different, random crystallographic orientations (no texture). However, for practical purposes, we artificially increase the share of GBs of a certain type in our finite element aggregate models, by imposing specific orientations to a relatively small fraction of grains.

In the continuum limit,⁴ a general GB type is defined by five independent parameters, which specify the orientations of two nearest grains relative to the GB plane. It can be expressed in the form of $[abc]$ - $[def]$ - $\Delta\omega$ GBs, where their GB-plane normal is the $[abc]$ direction in one grain and $[def]$ direction in the other grain, with $\Delta\omega$ denoting a relative twist of the two grain orientations about the GB normal.⁵

Due to topological constraints, not all GBs can be assigned the same GB character. In practice, a particular $[abc]$ - $[def]$ - $\Delta\omega$ GB type can be ascribed to at most $\sim 17\%$ of the GBs in a given aggregate, with the remaining GBs being of random type (*i.e.*, defined by two randomly oriented neighboring grains). A polycrystalline aggregate and two particular GB types are visualized in Fig. 1.

The constitutive equations of the generalized Hooke's law are solved numerically for a chosen uniform loading with FE solver Abaqus (Simulia, 2016). The obtained stresses σ , corresponding to the nearest integration points of a particular GB k , are then used to produce a single value $\sigma_{nn}(k)$ as their weighted average. Besides local stresses $\sigma_{nn}(k)$, first two statistical moments of PDF(σ_{nn}), the mean value and standard deviation, are calculated for the distribution of stresses on GBs of a chosen, overrepresented $[abc]$ - $[def]$ - $\Delta\omega$ GB type, whose density was artificially boosted (see Appendix A for further details).

Figs. 2 and 3 show typical (strong) effects of different GB types and different materials on both, local stresses σ_{nn} and the corresponding stress distributions PDF(σ_{nn}), for the assumed macroscopic uniaxial tensile loading Σ . In Fig. 2, a comparison of different $[abc]$ - $[def]$ GB types is made, with $\Delta\omega$ assumed random. Each value of GB index refers to a particular GB within the aggregate of fixed grain topology, shown in Fig. 1(a). In this way, the effect of the GB type can be isolated from other contributions. While the mean stress is independent of the GB type (with $\langle\sigma_{nn}\rangle = \Sigma/3$ for all types), the stress fluctuations are much larger on the (stiffest) [111]-[111] GBs than on the (softest) [001]-[001] GBs (El Shawish et al., 2021).

⁴ On the atomistic scale, more parameters would be required to characterize a GB by describing the arrangement of atoms on both sides of the GB plane (*e.g.*, coherent vs. non-coherent GBs).

⁵ GB type can also be defined by specifying less than five parameters. In such cases, the value of certain parameters can be assumed random. For example, misorientation GBs have only one fixed parameter and coincidence-site-lattice GBs, such as $\Sigma 3$, $\Sigma 5$, $\Sigma 7$, have three fixed parameters (El Shawish et al., 2021).

A similar behavior is observed in Fig. 3, where the effect of different material properties is isolated from other contributions by comparing σ_{nn} on identical GBs. All stress distributions PDF(σ_{nn}) are again centered around $\langle\sigma_{nn}\rangle = \Sigma/3$, while they are at the same time getting considerably wider with increasing grain anisotropy (El Shawish et al., 2021).

In most cases depicted in Figs. 2 and 3, a poor prediction capability of the isotropic model⁶ is observed, implying that local GB stresses are non-trivially dependent on the GB type, material properties and loading conditions.

3. Perturbative model of grain boundary normal stresses

3.1. Assumptions

To develop an accurate prediction for σ_{nn} (and the corresponding PDF(σ_{nn})), a step-by-step approach is taken, inspired by perturbation theory. In this sense, the solution for $\sigma_{nn}^{(k)}$, starting from the trivial isotropic-grain solution $\sigma_{nn}^{(0)}$, is refined in each successive step k by considering the contribution of more distant grains. To provide an analytic solution, sensible approximations and assumptions are used. For example, following Saint Venant's principle, the effects of more distant neighborhood on a GB are described in less detail, using only average quantities such as elastic grain anisotropy A^u (Ranganathan and Ostaja-Starzewski, 2008) or isotropic bulk stiffness $\langle E \rangle$. The strategy for building a perturbative model is shown schematically in Fig. 4. In the simplest approximation ($k = 0$), the neighborhood of a chosen GB can be modeled as isotropic, in which case the only relevant degree of freedom is the orientation of the GB plane. In the next order iteration ($k = 1$), the two (anisotropic) grains enclosing the GB are considered, while their combined (axial) strain is assumed equal as if both grains were made from (isotropic) bulk material.

This assumption works well for average grains, but the stiffer or softer the grains in the pair are, the more it starts to fail. To relax that condition, in the next order iteration ($k = 2$), "buffer" grains are introduced along the GB-normal (axial) direction. Then not only bicrystal pair, but the whole axial chain (containing also the buffer grains) is supposed to deform as if it was made from bulk material. In a similar manner, buffer grains are added also along the transverse directions, forming transverse chains of grains whose axial strain is constrained by the bulk ($k = 3$).

⁶ Isotropic model assumes isotropic material properties of the grains, resulting in local stresses that are equal to the applied stress.

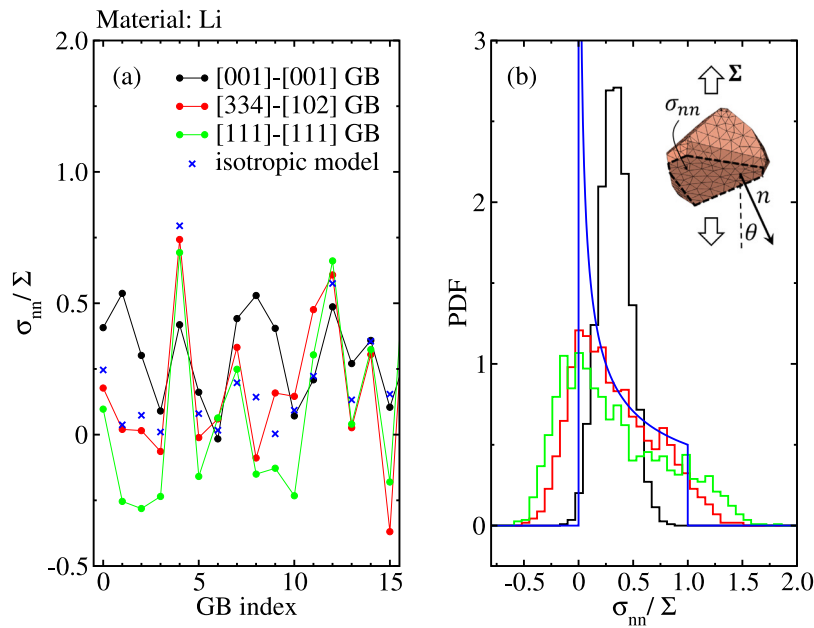


Fig. 2. (a) Normalized local stress responses σ_{nn} / Σ and (b) their statistical distributions $\text{PDF}(\sigma_{nn} / \Sigma)$ in a polycrystalline lithium under macroscopic tensile loading Σ for 3 different GB types. Large influence of a chosen GB type and poor prediction capability of the isotropic model ($\sigma_{nn} / \Sigma = \cos^2 \theta$) are clearly visible. In panel (a) the results are shown for just 15 randomly selected GBs of each type (GB index).

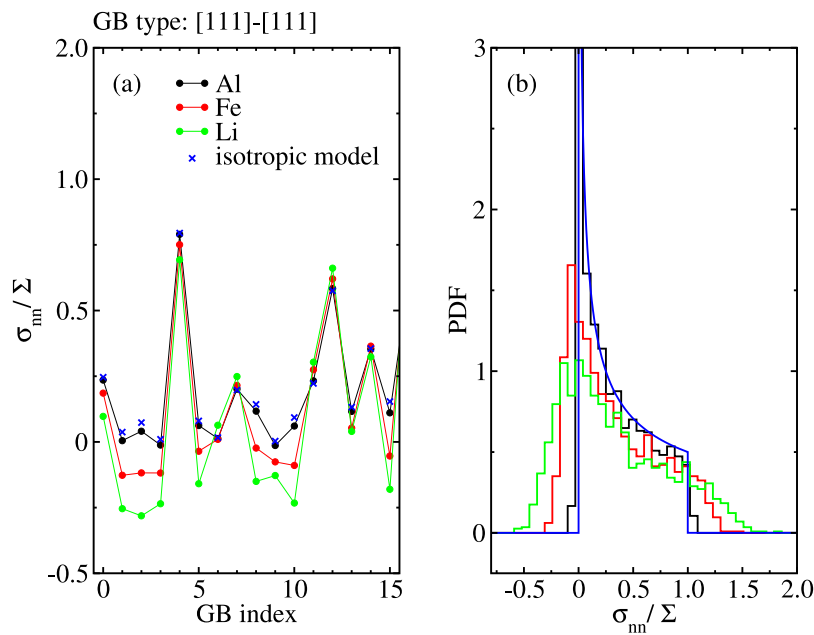


Fig. 3. Similarly as in Fig. 2, but evaluated on [111]-[111] GB type in different materials to demonstrate the effect of their elastic properties. Panel (b) shows how isotropic model begins to fail with the growing anisotropy of the grains.

In the isotropic-grain solution ($k = 0$), the GB-normal stress is equal to the externally applied stress projected onto a GB plane, $\sigma_{nn}^{(0)} = \Sigma_{zz}$, which for uniaxial loading Σ translates to $\sigma_{nn}^{(0)} = \Sigma \cos^2 \theta$, where θ is the angle between the GB normal and loading direction. The isotropic-grain solution may be a good initial approximation, but it turns to be a poor solution for moderate and highly anisotropic materials, see Figs. 2 and 3.

To obtain higher-order ($k > 0$) solutions $\sigma_{nn}^{(k)}$, the effect of two nearest grains enclosing the GB is considered in more detail, while the effect of more distant, buffer grains is accounted for less rigorously. Instead of a full 3D solution, several partial 1D solutions are obtained simultaneously and properly combined to accurately approximate $\sigma_{nn}^{(k)}$. Schematically, the corresponding general model can be viewed in

Fig. 5, as composed of one axial chain of length $L_n + 2$ and four lateral chains of length $L_l + 1$ crossing the two grains, that are adjacent to GB.

The chains are assumed decoupled from each other, but they interact with the surrounding bulk. The bulk is taken as isotropic, with average (bulk) properties, such as elastic stiffness $\langle E \rangle$ and Poisson's ratio $\langle \nu \rangle$. The chain-bulk interaction is, in the first approximation (*i.e.*, without lateral 3D coupling), assumed to be along the chain direction. It constrains the total strain of the chain to that of the isotropic bulk. This boundary condition corresponds to the Voigt-like assumption, but on a chain-length scale.

Buffer grains are assumed isotropic as well, but with elastic stiffness E_b and Poisson's ratio ν_b , both corresponding to the average response of a chain with L_n (or L_l) randomly oriented grains. However, when

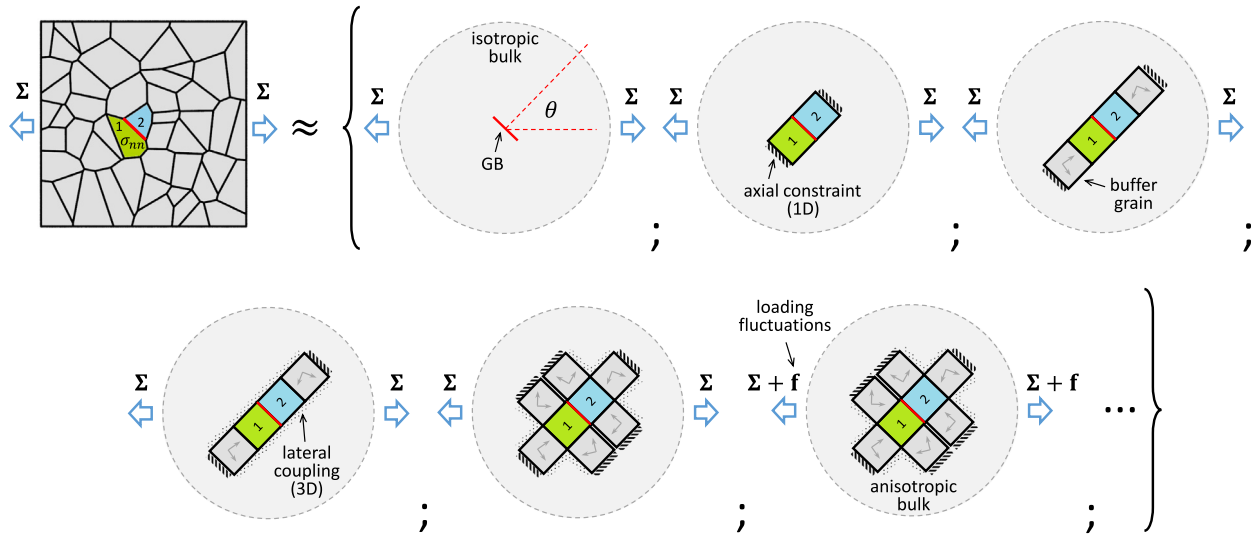


Fig. 4. Perturbation-theory based strategy for finding GB-normal stress $\sigma_{nn}^{(k)}$. In each successive step k , a more complex GB neighborhood is taken into account. For simplicity, the scheme presented here is only 2D and subjected to tensile loading Σ , but in practice a 3D case for a general uniform loading is considered.

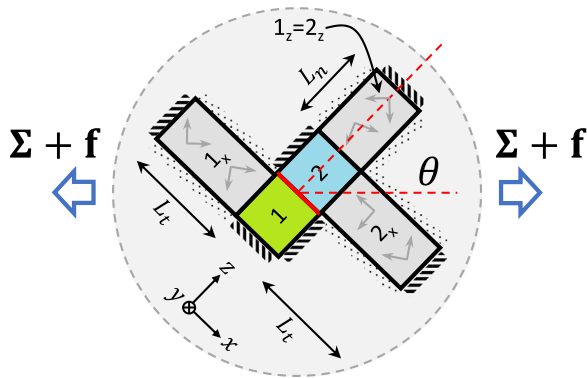


Fig. 5. A 2D sketch of perturbative model for GB stresses, consisting of two anisotropic grains of unit size, enclosing the GB, and several isotropic buffer grains of variable length, composing one axial chain of length $L_n + 2$ and two (four in 3D) transverse chains of length $L_t + 1$. Stresses and strains are assumed constant within the grains. Total strain of each chain is prescribed to match that of isotropic bulk of the same length and under the same external loading (Voigt-like assumption on a chain-length scale). 3D coupling of the chains with the surrounding bulk is modeled by assuming variable chain stiffness. External loading Σ is dressed by fluctuations f .

accounting for the lateral 3D effects (cf. Section 3.4.1), the chains are allowed to interact also laterally with the bulk and in the limit of long chains both parameters approach those of the bulk, $E_b \sim \langle E \rangle$ and $\nu_b \sim \langle \nu \rangle$.

The two grains on either side of the GB are assumed anisotropic, with their crystallographic orientations determining the $[abc]-[def]-\Delta\omega$ type of the corresponding GB.

Finally, the stresses and strains are considered homogeneous within all the grains. In addition, a general analytical expression for $\sigma_{nn}^{(k)}$ is derived by applying a reduced set of boundary conditions. To facilitate a simple, closed-form solution for $\sigma_{nn}^{(k)}$, only the conditions for stresses are imposed at the GB, while those for strains are neglected. Hence, the stress equilibrium is fulfilled everywhere in the model, while the strain compatibility at the GB is not guaranteed. These assumptions will be justified *a posteriori* by comparing the model results with those from numerical simulations.

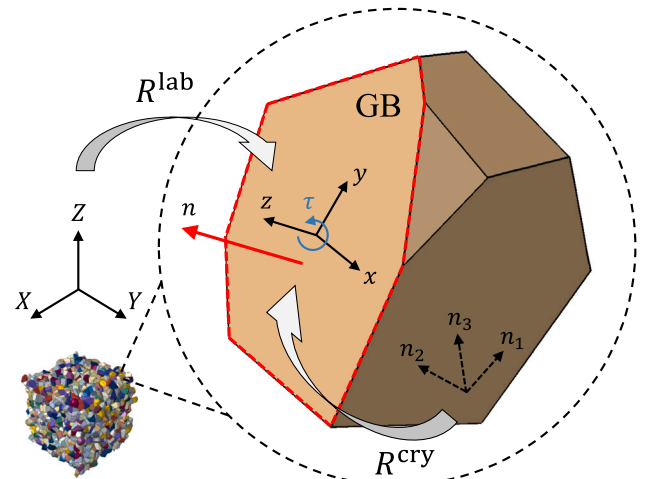


Fig. 6. Definition of three coordinate systems: laboratory coordinate system (X, Y, Z) , local-grain coordinate system (n_1, n_2, n_3) , and GB coordinate system (x, y, z) . The latter can be arbitrarily chosen with respect to the twist angle τ about the GB normal $\hat{n} \parallel \hat{z}$. Passive rotations \mathbf{R}^{lab} and \mathbf{R}^{cry} transform external and local-grain quantities, respectively, to the GB coordinate system. Since in the following, two grains will be considered, four coordinate systems will be in use, namely one crystallographic system for each grain, together with associated rotations $\mathbf{R}^{\text{cry},abc}$ and $\mathbf{R}^{\text{cry},def}$.

3.2. Analytical models

3.2.1. General setup

Analytical expressions for $\sigma_{nn}^{(k)}$ are presented in the GB coordinate system (x, y, z) with z -axis along the GB normal. All quantities expressed in the local-grain coordinate system (n_1, n_2, n_3) , aligned with crystallographic (eigen)-axes, and the laboratory coordinate system (X, Y, Z) , therefore need to be appropriately transformed using the following (passive) rotations \mathbf{R}^{cry} and \mathbf{R}^{lab} , respectively (see also Fig. 6),

$$\mathbf{R}^{\text{cry}}$$

$$= \begin{pmatrix} \frac{hl \cos \omega}{\sqrt{h^2+k^2}\sqrt{h^2+k^2+l^2}} - \frac{k \sin \omega}{\sqrt{h^2+k^2}} & \frac{kl \cos \omega}{\sqrt{h^2+k^2}\sqrt{h^2+k^2+l^2}} + \frac{h \sin \omega}{\sqrt{h^2+k^2}} & -\frac{\sqrt{h^2+k^2} \cos \omega}{\sqrt{h^2+k^2+l^2}} \\ \frac{hl \sin \omega}{\sqrt{h^2+k^2}\sqrt{h^2+k^2+l^2}} - \frac{k \cos \omega}{\sqrt{h^2+k^2}} & -\frac{kl \sin \omega}{\sqrt{h^2+k^2}\sqrt{h^2+k^2+l^2}} + \frac{h \cos \omega}{\sqrt{h^2+k^2}} & \frac{\sqrt{h^2+k^2} \sin \omega}{\sqrt{h^2+k^2+l^2}} \\ \frac{h}{\sqrt{h^2+k^2+l^2}} & \frac{k}{\sqrt{h^2+k^2+l^2}} & \frac{l}{\sqrt{h^2+k^2+l^2}} \end{pmatrix}, \quad (1)$$

$$\mathbf{R}^{\text{lab}} = \begin{pmatrix} \cos \theta \cos \psi \cos \phi - \sin \psi \sin \phi & \cos \theta \sin \psi \cos \phi + \cos \psi \sin \phi & -\sin \theta \cos \phi \\ -\cos \theta \cos \psi \sin \phi - \sin \psi \cos \phi & -\cos \theta \sin \psi \sin \phi + \cos \psi \cos \phi & \sin \theta \sin \phi \\ \sin \theta \cos \psi & \sin \theta \sin \psi & \cos \theta \end{pmatrix}. \quad (2)$$

While standard notation with three Euler angles (ψ, θ, ϕ), corresponding to a sequence of rotations \mathbf{R}_1 about \hat{n}_3 (angle ψ), \mathbf{R}_2 about $\mathbf{R}_1 \hat{n}_2$ (angle θ) and \mathbf{R}_3 about $\mathbf{R}_2 \mathbf{R}_1 \hat{n}_3 = \hat{z}$ (angle ϕ), is used for matrix \mathbf{R}^{lab} , the rotation \mathbf{R}^{cry} is expressed in terms of (h, k, l, ω) , where the GB normal corresponds to the $[hkl]$ direction⁷ in the local-grain coordinate system, and ω denotes a twist angle about the GB normal. This notation is particularly useful for analyzing the response of $[abc]$ - $[def]$ - $\Delta\omega$ GBs. In the following, we shall always use (x, y, z) to refer to the axes of the GB coordinate system and (X, Y, Z) for laboratory system associated with the external loading Σ . In this respect,

$$\Sigma^{\text{lab}} = \begin{pmatrix} \Sigma_{XX} & \Sigma_{XY} & \Sigma_{XZ} \\ \Sigma_{XY} & \Sigma_{YY} & \Sigma_{YZ} \\ \Sigma_{XZ} & \Sigma_{YZ} & \Sigma_{ZZ} \end{pmatrix}, \quad (3)$$

and

$$\Sigma^{\text{GB}} = \mathbf{R}^{\text{lab}} \Sigma^{\text{lab}} (\mathbf{R}^{\text{lab}})^T = \begin{pmatrix} \Sigma_{xx} & \Sigma_{xy} & \Sigma_{xz} \\ \Sigma_{xy} & \Sigma_{yy} & \Sigma_{yz} \\ \Sigma_{xz} & \Sigma_{yz} & \Sigma_{zz} \end{pmatrix}. \quad (4)$$

To find the solution of perturbative models in Fig. 4, the number of variables needs to match the number of boundary conditions. In isotropic limit, $\sigma_{ij}^{(0)} = \Sigma_{ij}$, and thus there are no constraints and no degrees of freedom. In a bicrystal model with (1D) axial constraint, there is only a single unknown ($\sigma_{zz}^{(1)} = \sigma_{zz}^{(2)}$), and also a single constraint on the axial strain ($\epsilon_{zz}^{(1)} + \epsilon_{zz}^{(2)} = 2\epsilon_{zz}^{\text{bulk}}$). The situation does not change even when buffer grains are added. For a (3D) model in Fig. 5, the following set of conditions is used, constraining the axial strains of all five 1D chains:

$$\begin{aligned} L_n \epsilon_{zz}^{(1z=2z)} + \epsilon_{zz}^{(1)} + \epsilon_{zz}^{(2)} &= (L_n + 2) \epsilon_{zz}^{\text{bulk}}, \\ L_t \epsilon_{xx}^{(1x)} + \epsilon_{xx}^{(1)} &= (L_t + 1) \epsilon_{xx}^{\text{bulk}}, \\ L_t \epsilon_{xx}^{(2x)} + \epsilon_{xx}^{(2)} &= (L_t + 1) \epsilon_{xx}^{\text{bulk}}, \\ L_t \epsilon_{yy}^{(1y)} + \epsilon_{yy}^{(1)} &= (L_t + 1) \epsilon_{yy}^{\text{bulk}}, \\ L_t \epsilon_{yy}^{(2y)} + \epsilon_{yy}^{(2)} &= (L_t + 1) \epsilon_{yy}^{\text{bulk}}. \end{aligned} \quad (5)$$

Strain of each grain is weighted by its length, i.e., either $L_n, L_t \geq 0$ for buffer grains, or 1 for unit-size GB grains. Superscript label of each strain-tensor component (and similarly for stresses) indicates to which particular grain it corresponds; $N = 1, 2$ for GB grains or N_i for buffer grains in $i = x, y, z$ directions.

Applying the generalized Hooke's law to GB grain N , the ii component of its strain tensor can be written as⁸

$$\begin{aligned} \epsilon_{ii}^{(N)} &= \sum_{k,l=1}^3 s_{iikl}^{\text{GB},N} \sigma_{kl}^{(N)} \\ &= \sum_{k,l,m,n,o,p=1}^3 R_{im}^{\text{cry},N} R_{in}^{\text{cry},N} R_{ko}^{\text{cry},N} R_{lp}^{\text{cry},N} s_{mnop}^{\text{cry}} \sigma_{kl}^{(N)}, \end{aligned} \quad (6)$$

with all stress-tensor components $\sigma_{kl}^{(N)}$ listed in Table 1. Note that shear stresses do not appear as variables in either grain, but have their values

⁷ The $[hkl]$ direction is determined by two (not three) independent parameters.

⁸ The summation indices 1, 2, 3 correspond to x, y, z , respectively.

Table 1

Assumed stress components in different grains of the model. Buffer grain label N_i denotes the corresponding GB grain ($N = 1, 2$) and the direction of the chain, to which it belongs ($i = x, y, z$).

Grain	Assigned stresses	Unknown stresses
GB grain 1	$\sigma_{ij}^{(1)} = \Sigma_{ij}, i \neq j$	$\sigma_{xx}^{(1)}, \sigma_{yy}^{(1)}, \sigma_{zz}^{(1)}$
GB grain 2	$\sigma_{ij}^{(2)} = \Sigma_{ij}, i \neq j$	$\sigma_{xx}^{(2)}, \sigma_{yy}^{(2)}, \sigma_{zz}^{(2)} = \sigma_{zz}^{(1)}$
buffer 1 _x	$\sigma_{ij}^{(1_x)} = \Sigma_{ij}, ij \neq xx$	$\sigma_{xx}^{(1_x)} = \sigma_{xx}^{(1)}$
buffer 1 _y	$\sigma_{ij}^{(1_y)} = \Sigma_{ij}, ij \neq yy$	$\sigma_{yy}^{(1_y)} = \sigma_{yy}^{(1)}$
buffer 2 _x	$\sigma_{ij}^{(2_x)} = \Sigma_{ij}, ij \neq xx$	$\sigma_{xx}^{(2_x)} = \sigma_{xx}^{(2)}$
buffer 2 _y	$\sigma_{ij}^{(2_y)} = \Sigma_{ij}, ij \neq yy$	$\sigma_{yy}^{(2_y)} = \sigma_{yy}^{(2)}$
buffer 1 _z (= 2 _z)	$\sigma_{ij}^{(1_z)} = \Sigma_{ij}, ij \neq zz$	$\sigma_{zz}^{(1_z)} = \sigma_{zz}^{(1)}$

assigned ($\sigma_{ij}^{(N)} = \Sigma_{ij}$ for $i \neq j$), i.e., they are set equal to the components of external-stress tensor, rotated to a local GB system; cf. Eq. (4). Out of the 6 remaining stress components in both grains, two are set equal due to stress-continuity condition ($\sigma_{zz}^{(1)} = \sigma_{zz}^{(2)} := \sigma_{zz}$), hence the number of unknowns (five) matches the number of constraints in Eq. (5).

Compliance tensor s^{cry} , expressed in the local (crystallographic) coordinate system of the grain, is readily transformed to the GB system, where rotation matrices \mathbf{R}^{cry} can be different for both grains. Depending on the symmetry of the grain lattice, s^{cry} can be expressed as a function of minimum two (isotropic) and maximum 21 (triclinic) independent elastic parameters. Here, no preference for the underlying symmetry is assumed, thus keeping the approach as general as possible.

To maintain the clarity of the manuscript, only functional dependence of $\epsilon_{ii}^{(N)}$ is retained here⁹ (with full analytic expressions for cubic lattice symmetry presented in Appendix B),

$$\begin{aligned} \epsilon_{ii}^{(1)} &= \mathcal{F}(s^{\text{cry}}; a, b, c, \omega_1; \sigma_{xx}^{(1)}, \sigma_{yy}^{(1)}, \sigma_{zz}, \Sigma_{xy}, \Sigma_{xz}, \Sigma_{yz}), \\ \epsilon_{ii}^{(2)} &= \mathcal{F}(s^{\text{cry}}; d, e, f, \omega_2; \sigma_{xx}^{(2)}, \sigma_{yy}^{(2)}, \sigma_{zz}, \Sigma_{xy}, \Sigma_{xz}, \Sigma_{yz}). \end{aligned} \quad (7)$$

Generic (h, k, l, ω) parameters in \mathbf{R}^{cry} have been replaced by specific values (a, b, c, ω_1) and (d, e, f, ω_2) in GB grains 1 and 2, respectively. This setting corresponds to a well-defined GB type $[abc]$ - $[def]$ - $\Delta\omega$ with $\Delta\omega := \omega_2 - \omega_1$.

Similar expressions apply also to buffer grains N_i . The only difference is that there all stress components correspond to projected external loading Σ^{GB} . The only exception is the axial stress $\sigma_{ii}^{(N_i)}$, which matches $\sigma_{ii}^{(N)}$ in GB grain N due to stress-continuity along the chain length. Stress components in each of the grains are summarized in Table 1.

Sufficiently far from the GB, the grains can be treated as isotropic. This allows for much simpler expressions for strain components ϵ_{ii} (with $i = x, y, z$) in both, buffer grains and the bulk material,

$$\epsilon_{ii}^{(N_i)} = \frac{1}{E_b} \left(\sigma_{ii}^{(N)} - \nu_b (\text{tr}(\Sigma^{\text{GB}}) - \Sigma_{ii}) \right), \quad (8)$$

$$\epsilon_{ii}^{\text{bulk}} = \frac{1}{\langle E \rangle} \left(\Sigma_{ii} - \langle \nu \rangle (\text{tr}(\Sigma^{\text{GB}}) - \Sigma_{ii}) \right). \quad (9)$$

With relevant strain components in individual grains defined in Eqs. (7), (8) and (9), the set of conditions in Eq. (5), constraining the axial strains of all five chains, can be solved analytically for all five unknown stresses $\sigma_{ii}^{(N)}$, including the GB-normal stress $\sigma_{nn} := \sigma_{zz}$.

However, the resulting σ_{nn} has a significant deficiency. It depends on the choice of the local GB coordinate system (the value of twist angle τ in Fig. 6). This dependence originates in the prescribed directions of the four lateral chains, which are directed along the local x and y axes. A different choice of x and y axes would produce different

⁹ Parameters in \mathcal{F} are grouped into three sets, separated by semicolons. They are related either to material properties, GB orientation or loading.

lateral constraints, which would result in a different σ_{nn} . To avoid this ambiguity, a symmetrized lateral boundary condition is derived below.

3.2.2. Symmetrized model

The model is symmetrized by averaging the lateral boundary condition over all possible GB coordinate systems. The twist of the local GB system for an arbitrary angle τ about the GB normal (z -axis) changes how Σ^{GB} and $s^{\text{GB},N}$ are expressed in that system. Specifically, the rotation changes the Euler angles ω_N and ϕ in transformation matrices (1) and (2), respectively,

$$\begin{aligned} \omega_N &\rightarrow \omega_N + \tau; \quad (N = 1, 2), \\ \phi &\rightarrow \phi + \tau, \end{aligned} \quad (10)$$

which in turn affect Eqs. (7), (8) and (9), and make them τ dependent. Since all twist rotations should be equivalent, averaging over τ replaces Eq. (5) with new, symmetrized boundary conditions

$$\begin{aligned} \frac{1}{2\pi} \int_0^{2\pi} \left(L_n \epsilon_{zz}^{(1, z=2z)} + \epsilon_{zz}^{(1)} + \epsilon_{zz}^{(2)} \right) d\tau &= \frac{1}{2\pi} \int_0^{2\pi} (L_n + 2) \epsilon_{zz}^{\text{bulk}} d\tau, \\ \frac{1}{2\pi} \int_0^{2\pi} \left(L_t \epsilon_{xx}^{(1, x)} + \epsilon_{xx}^{(1)} \right) d\tau &= \frac{1}{2\pi} \int_0^{2\pi} (L_t + 1) \epsilon_{xx}^{\text{bulk}} d\tau, \\ \frac{1}{2\pi} \int_0^{2\pi} \left(L_t \epsilon_{xx}^{(2, x)} + \epsilon_{xx}^{(2)} \right) d\tau &= \frac{1}{2\pi} \int_0^{2\pi} (L_t + 1) \epsilon_{xx}^{\text{bulk}} d\tau, \\ \frac{1}{2\pi} \int_0^{2\pi} \left(L_t \epsilon_{yy}^{(1, y)} + \epsilon_{yy}^{(1)} \right) d\tau &= \frac{1}{2\pi} \int_0^{2\pi} (L_t + 1) \epsilon_{yy}^{\text{bulk}} d\tau, \\ \frac{1}{2\pi} \int_0^{2\pi} \left(L_t \epsilon_{yy}^{(2, y)} + \epsilon_{yy}^{(2)} \right) d\tau &= \frac{1}{2\pi} \int_0^{2\pi} (L_t + 1) \epsilon_{yy}^{\text{bulk}} d\tau. \end{aligned} \quad (11)$$

Solving the above set of symmetrized equations for five unknowns $\sigma_{ii}^{(N)}$ (with $i = x, y, z$ and $N = 1, 2$), provides analytical $\sigma_{nn} := \sigma_{zz}$, independent of τ . However, for the most general case the resulting expression is too cumbersome to be presented here. Hence, we again resort to its functional dependence

$$\begin{aligned} \sigma_{nn} &= \mathcal{F}(s^{\text{crv}}, \langle E \rangle, \langle \nu \rangle, E_b, \nu_b; a, b, c, \omega_1, d, e, f, \omega_2; L_n, L_t; \Sigma^{\text{GB}}) \\ &= \mathcal{F}(s^{\text{crv}}, \langle E \rangle, \langle \nu \rangle, E_b, \nu_b; a, b, c, \omega_1 - \phi, d, e, f, \omega_2 - \phi; L_n, L_t; \\ &\quad \Sigma^{\text{lab}}, \theta, \psi), \end{aligned} \quad (12)$$

from which it is clear, that σ_{nn} does not depend on the choice of the GB coordinate system due to observed $\omega_1 - \phi$ and $\omega_2 - \phi$ dependence. The normal stress σ_{nn} is a complicated function of many parameters¹⁰ (e.g., up to 39 independent parameters in a material with triclinic lattice symmetry and for a most general external loading). However, not all parameters are of same significance, as shown in Section 3.3, where σ_{nn} is tested against numerical results. In order to derive a compact, but still meaningful expression, further approximations are needed.

So far, the strategy was based on adding more complexity to the model when getting closer to the GB. In this respect, grains closest to it have been modeled in greater detail (e.g., employing anisotropic elasticity and mostly unknown loading conditions), while the grains further away required less modeling (e.g., employing isotropic elasticity and mostly known loading conditions).

With the goal to provide a compact and accurate analytical expression for σ_{nn} (and the corresponding PDF(σ_{nn})), few selected limits of the general result, Eq. (12), are investigated and discussed in more detail. Some of these limits will become very useful later, when a comparison with the numerical results is done in Section 3.3.

3.2.3. Isotropic limit ($k = 0$)

The initial (zeroth order) approximation $\sigma_{nn}^{(0)}$, representing the exact solution in the isotropic material limit, can be reproduced from Eq. (12)

¹⁰ To account for loading fluctuations due to anisotropy of the bulk, a universal elastic anisotropy index A^u should be added to the list of influencing parameters (see Section 3.4.2). On the other hand, A^u , $\langle E \rangle$ and $\langle \nu \rangle$ are all only functions of s^{crv} .

in two ways, either by assuming isotropic properties of the grains (i.e., by taking the appropriate s^{crv}) or taking the limit of very long chains ($L_n, L_t \rightarrow \infty$) with average properties ($E_b = \langle E \rangle$, $\nu_b = \langle \nu \rangle$), in which the chain-strain constraints become ineffective, resulting in stresses equal to external loading,

$$\begin{aligned} \sigma_{nn}^{(0)} &= \Sigma_{zz} \\ &= \Sigma_{XX} \sin^2 \theta \cos^2 \psi + \Sigma_{YY} \sin^2 \theta \sin^2 \psi + \Sigma_{ZZ} \cos^2 \theta \\ &\quad + \Sigma_{XY} \sin^2 \theta \sin 2\psi + \Sigma_{XZ} \sin 2\theta \cos \psi + \Sigma_{YZ} \sin 2\theta \sin \psi. \end{aligned} \quad (13)$$

Having a sufficient number of GBs with normals uniformly distributed on a sphere, the corresponding first two statistical moments of PDF($\sigma_{nn}^{(0)}$), the mean value and standard deviation, can be straightforwardly expressed as

$$\begin{aligned} \langle \sigma_{nn}^{(0)} \rangle &= \frac{1}{3} \text{tr}(\Sigma^{\text{lab}}), \\ s(\sigma_{nn}^{(0)}) &= \frac{2}{3\sqrt{5}} \Sigma_{\text{mis}}^{\text{lab}}, \end{aligned} \quad (14)$$

where $\frac{1}{3} \text{tr}(\Sigma^{\text{lab}})$ is a hydrostatic pressure, related to volume change of the aggregate, and $\Sigma_{\text{mis}}^{\text{lab}}$ corresponds to von Mises external stress, traditionally associated with the yielding of ductile materials. Von Mises stress is related to deviatoric tensor (responsible for volume preserving shape changes of the aggregate),

$$\begin{aligned} \Sigma_{\text{mis}}^{\text{lab}} &:= \frac{\sqrt{3}}{\sqrt{2}} \sqrt{\text{tr}((\Sigma_{\text{dev}}^{\text{lab}})^2)}, \\ \Sigma_{\text{dev}}^{\text{lab}} &:= \Sigma^{\text{lab}} - \frac{1}{3} \text{tr}(\Sigma^{\text{lab}}) \mathbb{1}_{3 \times 3}. \end{aligned} \quad (15)$$

Both, $\text{tr}(\Sigma^{\text{lab}})$ and $\Sigma_{\text{mis}}^{\text{lab}}$ are rotational invariants and thus assume identical form in all coordinate systems.

Even though Eq. (14) is derived for isotropic case ($k = 0$), the same functional dependence of the first two statistical moments on Σ^{lab} is retained for all orders k , suggesting that the loading part can be trivially decoupled from the material and GB-type contributions. In a specific case, when the external stress is of hydrostatic form (i.e., proportional to identity matrix; $\Sigma^{\text{lab}} := \Sigma_0 \mathbb{1}_{3 \times 3}$), this can be easily confirmed. In that case, there is no effect of grain orientations, since stress tensor is invariant to rotations. Hence, the trivial (hydrostatic) solution applies to the whole aggregate ($\sigma_{nn}^{(k)} = \Sigma_0$), resulting in an infinitely narrow stress (and strain) distribution. On the other hand $\Sigma_{\text{mis}}^{\text{lab}} = 0$, therefore $s(\sigma_{nn}) \sim \Sigma_{\text{mis}}^{\text{lab}}$ applies for any, not just isotropic material.

3.2.4. Axially constrained bicrystal ($k = 1$)

The first non-trivial solution $\sigma_{nn}^{(1)}$ corresponds to a bicrystal, embedded axially in the isotropic bulk ($L_n \rightarrow 0$). As there are no lateral constraints imposed on the two GB grains, this model corresponds to the $L_t \rightarrow \infty$ limit of the general model shown in Fig. 5. However, to obtain a compact expression for $\sigma_{nn}^{(1)}$, another simplification is required, which will be justified in Section 3.3. Since we are interested in the response of $[abc]$ - $[def]$ - $\Delta\omega$ GBs, which have a well-defined difference of the two twist angles, $\sigma_{nn}^{(1)}$ is obtained by replacing ω_2 in Eq. (12) with $\omega_1 + \Delta\omega$, and averaging it over ω_1 :

$$\begin{aligned} \sigma_{nn}^{(1)} &:= \frac{1}{2\pi} \int_0^{2\pi} \left(\lim_{\substack{L_n \rightarrow 0 \\ L_t \rightarrow \infty}} \sigma_{nn} \right)_{\omega_2 = \omega_1 + \Delta\omega} d\omega_1 \\ &= E_{12} \Sigma_{zz} + E_{12} (\nu_{12} - \langle \nu \rangle) (\Sigma_{xx} + \Sigma_{yy}), \end{aligned} \quad (16)$$

where

$$\begin{aligned} E_{12} &= \frac{2 \langle E \rangle^{-1}}{E_{abc}^{-1} + E_{def}^{-1}} = \frac{2 \langle E \rangle^{-1}}{s_{3333}^{\text{GB}, abc} + s_{3333}^{\text{GB}, def}}, \\ \nu_{12} &= -\frac{\langle E \rangle}{4} \left(s_{3311}^{\text{GB}, abc} + s_{3322}^{\text{GB}, abc} + s_{3311}^{\text{GB}, def} + s_{3322}^{\text{GB}, def} \right), \end{aligned} \quad (17)$$

and

$$s_{33jj}^{GB,hkl} = \sum_{m,n,o,p=1}^3 R_{3m}^{cry,hkl} R_{3n}^{cry,hkl} R_{jo}^{cry,hkl} R_{jp}^{cry,hkl} s_{mnop}^{cry}, \quad (18)$$

for $j = 1, 2, 3$ and $hkl = abc$ or def . This approximation removes (averages out) all the twist-angle degrees of freedom. We will refer to it as the *reduced* version of the model, intended to mimic the behavior observed in numerical studies. The derived compact expression for $\sigma_{nn}^{(1)}$ is the first main result of this study. It suggests that GB-normal stress is a simple function of the loading part, contained in Σ_{xx} , Σ_{yy} and Σ_{zz} , and the GB-type (and material) part, which is represented compactly by only two (composite) parameters E_{12} and ν_{12} . While E_{12} has already been introduced in El Shawish et al. (2021) as an effective GB stiffness, measuring the average stiffness of GB neighborhood along the GB-normal direction, the newly introduced ν_{12} can be seen as an effective GB Poisson's ratio, measuring the average ratio of transverse and axial responses (strains) in both GB grains. Both E_{12} and ν_{12} are unitless and characterize the $[abc]$ - $[def]$ - $\Delta\omega$ GB neighborhood in terms of local material and GB-type parameters,¹¹

$$E_{12} = \mathcal{F}(s^{cry}, \langle E \rangle, a, b, c, d, e, f), \quad (19)$$

$$\nu_{12} = \mathcal{F}(s^{cry}, \langle E \rangle, a, b, c, d, e, f). \quad (20)$$

Full analytic expressions for E_{12} and ν_{12} (as well as $\langle E \rangle$ and $\langle \nu \rangle$) depend on the choice of the grain lattice symmetry (expressions for cubic lattice symmetry are given in Appendix B). Note that expressions simplify considerably with more symmetric lattices. In cubic lattices, for example, a GB is fully characterized by E_{12} alone, since $\nu_{12} = \langle \nu \rangle + \frac{1}{2}(E_{12}^{-1} - 1)$. In isotropic grains, $E_{12} = 1$ and $\nu_{12} = \langle \nu \rangle$, which recovers the $\sigma_{nn}^{(0)}$ solution.

Switching to a statistical behavior of infinitely many $[abc]$ - $[def]$ - $\Delta\omega$ GBs with randomly oriented GB planes, the first two statistical moments of PDF($\sigma_{nn}^{(1)}$), the mean value and standard deviation, become

$$\begin{aligned} \langle \sigma_{nn}^{(1)} \rangle &= \frac{\text{tr}(\Sigma^{\text{lab}})}{3} E_{12} (1 + 2(\nu_{12} - \langle \nu \rangle)), \\ s(\sigma_{nn}^{(1)}) &= \frac{2}{3\sqrt{5}} \Sigma_{\text{mis}}^{\text{lab}} E_{12} \sqrt{(1 - \nu_{12} + \langle \nu \rangle)^2}. \end{aligned} \quad (21)$$

For cubic lattices they simplify to $\langle \sigma_{nn}^{(1)} \rangle = \text{tr}(\Sigma^{\text{lab}})/3$ and $s(\sigma_{nn}^{(1)}) = \Sigma_{\text{mis}}^{\text{lab}}/(3\sqrt{5})|1 - 3E_{12}|$. The fact that the mean stress is equal to $\Sigma/3$ for the uniaxial loading Σ , while the fluctuation of GB-normal stress in cubic grains is a monotonic function of a single GB parameter E_{12} (although the functional dependence differs from that of Eq. (21)), has already been identified in (realistic) FE simulations (El Shawish et al., 2021). However, the observed behavior can now be easily extended to other non-cubic lattices and for general external loading. The accuracy of the derived expressions for local $\sigma_{nn}^{(1)}$, Eqs. (16)–(17), and statistical PDF($\sigma_{nn}^{(1)}$), Eq. (21), is investigated in more detail in Section 3.3.

3.2.5. Axially constrained chain with $L_n + 2$ grains ($k = 2$)

The next-order solution $\sigma_{nn}^{(2)}$ corresponds to a single chain with $L_n + 2$ grains, axially constrained by the isotropic bulk. The reason for adding a buffer grain of length $L_n > 0$ to the bicrystal is to relax the axial strain constraint. In the previous ($k = 1$) iteration, this constraint applies directly to the bicrystal, which produces too large (resp. small) stresses $\sigma_{nn}^{(1)}$ on very stiff (resp. soft) GBs, see Section 3.3.

Following the same reasoning and steps as in the bicrystal model, the resulting *reduced* version is derived for a general grain-lattice

symmetry and arbitrary external loading

$$\begin{aligned} \sigma_{nn}^{(2)} &:= \frac{1}{2\pi} \int_0^{2\pi} \left(\lim_{L_t \rightarrow \infty} \sigma_{nn} \right) \Big|_{\omega_2=\omega_1+\Delta\omega} d\omega_1 \\ &= \frac{2 + L_n}{2E_{12}^{-1} + L_n E_3^{-1}} \Sigma_{zz} \\ &\quad + \frac{2}{2E_{12}^{-1} + L_n E_3^{-1}} \left(\nu_{12} - \langle \nu \rangle - \frac{1}{2} L_n (\langle \nu \rangle - \nu_b E_3^{-1}) \right) (\Sigma_{xx} + \Sigma_{yy}) \\ &\approx \frac{2 + L_n}{2E_{12}^{-1} + L_n} \Sigma_{zz} + \frac{2(\nu_{12} - \langle \nu \rangle)}{2E_{12}^{-1} + L_n} (\Sigma_{xx} + \Sigma_{yy}). \end{aligned} \quad (22)$$

Same definitions for E_{12} and ν_{12} apply as in Eq. (17), while $E_3 := E_b/\langle E \rangle$ and ν_b denote, respectively, the normalized elastic stiffness and Poisson's ratio of the (isotropic) buffer grain. Its response corresponds to the average response of a chain with L_n randomly oriented grains

$$\begin{aligned} E_b &:= E_{L_n}^{\text{rnd}} = \left\langle \frac{L_n}{\sum_i s_{3333}^{\text{GB},i}} \right\rangle_{L_n}, \\ \nu_b &:= \nu_{L_n}^{\text{rnd}} = - \left\langle \frac{\sum_i s_{1133}^{\text{GB},i}}{\sum_i s_{3333}^{\text{GB},i}} \right\rangle_{L_n}. \end{aligned} \quad (23)$$

The averaging $\langle \dots \rangle_{L_n}$ is assumed over all possible linear configurations of L_n grains with random orientations, and the summation index i runs over the grains in each chain.

The elastic response of a buffer grain, calculated in this way, is usually softer than that of the bulk ($E_3 < 1$). Nevertheless, it is convenient to assume $E_3 \approx 1$ and $\nu_b \approx \langle \nu \rangle$. In fact, this assumption becomes realistic, when the 3D effects are considered, e.g., the lateral coupling of buffer grain to the neighboring bulk (see Section 3.4.1).

Assuming $E_3 = 1$ and $\nu_b = \langle \nu \rangle$, the mean value and standard deviation of PDF($\sigma_{nn}^{(2)}$) become

$$\begin{aligned} \langle \sigma_{nn}^{(2)} \rangle &= \frac{\text{tr}(\Sigma^{\text{lab}})}{3} \frac{2 + L_n + 4(\nu_{12} - \langle \nu \rangle)}{2E_{12}^{-1} + L_n}, \\ s(\sigma_{nn}^{(2)}) &= \frac{2}{3\sqrt{5}} \frac{\Sigma_{\text{mis}}^{\text{lab}} \sqrt{(2 + L_n - 2(\nu_{12} - \langle \nu \rangle))^2}}{2E_{12}^{-1} + L_n}, \end{aligned} \quad (24)$$

which simplify for cubic lattices to $\langle \sigma_{nn}^{(2)} \rangle = \text{tr}(\Sigma^{\text{lab}})/3$, $s(\sigma_{nn}^{(2)}) = 2\Sigma_{\text{mis}}^{\text{lab}}/(3\sqrt{5})\sqrt{((3 + L_n) - E_{12}^{-1})^2/(2E_{12}^{-1} + L_n)}$.

In contrast to the bicrystal model, the $\sigma_{nn}^{(2)}$ expression depends also on the parameter L_n , which makes it a mixture of bicrystal solution $\sigma_{nn}^{(1)}$ (reproduced for $L_n \rightarrow 0$) and isotropic solution $\sigma_{nn}^{(0)}$ (reproduced for $L_n \rightarrow \infty$). However, the effect of L_n is negligible for GBs with $E_{12} \sim 1$ and $\nu_{12} \sim \langle \nu \rangle$. As shown in Section 3.3, the value $L_n \sim 2$ best replicates the numerical results.

3.2.6. Axially constrained chains with $L_n + 2$ and $L_t + 1$ grains ($k = 3$)

The highest-order solution considered in this study is $\sigma_{nn}^{(3)}$. It corresponds to the complex configuration of chains, shown in Fig. 5. The axial chain consists of $L_n + 2$ grains and the four transverse chains of $L_t + 1$ grains. All the chains are assumed to be axially constrained to the strain of isotropic bulk of equal length. In a similar fashion to previous iterations, the *reduced* version can be derived for a general grain-lattice symmetry and arbitrary external loading

$$\begin{aligned} \sigma_{nn}^{(3)} &:= \frac{1}{2\pi} \int_0^{2\pi} \sigma_{nn} \Big|_{\omega_2=\omega_1+\Delta\omega} d\omega_1 \\ &= A^{(3)} \Sigma_{zz} + B^{(3)} (\Sigma_{xx} + \Sigma_{yy}), \end{aligned} \quad (25)$$

where, assuming $E_3 = 1$ and $\nu_b = \langle \nu \rangle$ (see Eq. (26) in Box I),

¹¹ With the exception of $\Delta\omega$, whose influence is implicitly removed from Eq. (16) by integration over ω_1 .

$$\begin{aligned}
A^{(3)} &= \frac{(2 + L_n)(s_{tt}^{abc} + \langle E \rangle^{-1} L_t)(s_{tt}^{def} + \langle E \rangle^{-1} L_t) + \langle \nu \rangle ((s_{tt}^{abc} + \langle E \rangle^{-1} L_t)s_{tt}^{def} + (s_{tt}^{def} + \langle E \rangle^{-1} L_t)s_{tt}^{abc})}{(2E_{12}^{-1} + L_n)(s_{tt}^{abc} + \langle E \rangle^{-1} L_t)(s_{tt}^{def} + \langle E \rangle^{-1} L_t) - \frac{1}{2} \langle E \rangle ((s_{tt}^{abc} + \langle E \rangle^{-1} L_t)(s_{tt}^{def})^2 + (s_{tt}^{def} + \langle E \rangle^{-1} L_t)(s_{tt}^{abc})^2)}, \\
B^{(3)} &= -\frac{2 \langle \nu \rangle (s_{tt}^{abc} + \langle E \rangle^{-1} L_t)(s_{tt}^{def} + \langle E \rangle^{-1} L_t) + \frac{1}{2} (1 + L_t - \langle \nu \rangle)((s_{tt}^{abc} + \langle E \rangle^{-1} L_t)s_{tt}^{def} + (s_{tt}^{def} + \langle E \rangle^{-1} L_t)s_{tt}^{abc})}{(2E_{12}^{-1} + L_n)(s_{tt}^{abc} + \langle E \rangle^{-1} L_t)(s_{tt}^{def} + \langle E \rangle^{-1} L_t) - \frac{1}{2} \langle E \rangle ((s_{tt}^{abc} + \langle E \rangle^{-1} L_t)(s_{tt}^{def})^2 + (s_{tt}^{def} + \langle E \rangle^{-1} L_t)(s_{tt}^{abc})^2)},
\end{aligned} \tag{26}$$

Box I.

Table 2

A summary of derived models. Analytical solutions can be written in a compact form only in certain limits.

k	Model	Version ^a	Assumptions ^b	Fitting parameters	Compact solution ^c
0	isotropic	full	$A^u = 0$ or $L_n, L_t \rightarrow \infty$	–	$\sigma_{nn}^{(0)} = \mathcal{F}(\Sigma^{GB})$
1	bicrystal	full	$L_n \rightarrow 0, L_t \rightarrow \infty$	–	–
		reduced	$L_n \rightarrow 0, L_t \rightarrow \infty, \int d\omega_1 _{\omega_2=\omega_1+\Delta\omega}$	–	$\sigma_{nn}^{(1)} = \mathcal{F}(\Sigma^{GB}, E_{12}, \nu_{12}, \langle E \rangle, \langle \nu \rangle)$
2	L_n -chain	full	$L_t \rightarrow \infty$	$L_n \geq 0$	–
		reduced	$L_t \rightarrow \infty, \int d\omega_1 _{\omega_2=\omega_1+\Delta\omega}$	$L_n \geq 0$	$\sigma_{nn}^{(2)} = \mathcal{F}(\Sigma^{GB}, E_{12}, \nu_{12}, \langle E \rangle, \langle \nu \rangle, L_n)$
3	$L_n - L_t$ -chain	full	–	$L_n, L_t \geq 0$	–
		reduced	$\int d\omega_1 _{\omega_2=\omega_1+\Delta\omega}$	$L_n, L_t \geq 0$	$\sigma_{nn}^{(3)} = \mathcal{F}(\Sigma^{GB}, s_{tt}^{abc}, s_{tt}^{def}, s_{tt}^{def}, s_{tt}^{def}, \langle E \rangle, \langle \nu \rangle, L_n, L_t)$

^aIn contrast to the full version, the reduced version of the model eliminates the twist-angle degrees of freedom, which makes the solution only approximate, but significantly more condensed. Note that both versions provide the same mean value $\langle \sigma_{nn}^{(k)} \rangle$.

^bAssumptions are taken with respect to the general solution; cf. Eq. (12).

^cCompact solutions are derived for a general grain-lattice symmetry.

for

$$\begin{aligned}
s_{tt}^{hkl} &:= \frac{1}{2} (s_{1111}^{GB,hkl} + s_{2222}^{GB,hkl}) + s_{1122}^{GB,hkl}, \\
s_{tl}^{hkl} &:= s_{1133}^{GB,hkl} + s_{2233}^{GB,hkl}, \\
s_{ll}^{hkl} &:= s_{3333}^{GB,hkl} := E_{hkl}^{-1}.
\end{aligned} \tag{27}$$

The combinations of compliance-tensor components,¹² introduced in Eq. (27), are related through a material dependent (but GB type independent) linear combination

$$2s_{tt}^{hkl} + 2s_{tl}^{hkl} + s_{ll}^{hkl} = (s_{1111}^{cry} + s_{2222}^{cry} + s_{3333}^{cry}) + 2(s_{1122}^{cry} + s_{1133}^{cry} + s_{2233}^{cry}), \tag{28}$$

which suggests that $\sigma_{nn}^{(3)}$ is a function of (at most) four local GB parameters (in addition to bulk properties $\langle E \rangle$, $\langle \nu \rangle$ and chain parameters L_n, L_t). In the $L_t \rightarrow \infty$ limit, $\sigma_{nn}^{(3)}$ reduces to $\sigma_{nn}^{(2)}$, see Eq. (22).

The corresponding first two statistical moments can also be expressed analytically (but they are not shown here for brevity). They have the already familiar loading dependence,

$$\begin{aligned}
\langle \sigma_{nn}^{(3)} \rangle &\sim \frac{\text{tr}(\Sigma^{\text{lab}})}{3}, \\
s(\sigma_{nn}^{(3)}) &\sim \frac{2\Sigma_{\text{mis}}^{\text{lab}}}{3\sqrt{5}}.
\end{aligned} \tag{29}$$

Expressions simplify further for higher lattice symmetries. For cubic lattices, for example, $A^{(3)}$ and $B^{(3)}$ become (again) only functions of Young's moduli E_{abc} and E_{def} along the GB-normal direction (see Appendix C).¹³

All compact-form solutions $\sigma_{nn}^{(k)}$, representing the special limits of the general solution, Eq. (12), are summarized in Table 2.

¹² The compliance-tensor components $s_{ijkl}^{GB,hkl}$ depend on the twist angle ω , but their linear combinations, defined in Eq. (27), do not. Hence, the reduced model solution $\sigma_{nn}^{(3)}$ in Eq. (25) is indeed independent of $\Delta\omega$.

¹³ For cubic lattices, the E_{abc} and E_{def} parameters appear in a single combination (E_{12}) in $\sigma_{nn}^{(1)}$ and $\sigma_{nn}^{(2)}$, while in $\sigma_{nn}^{(3)}$ there are two such combinations (E_{12} and Δ_{12}), see Appendix C.

3.3. Models validation

In this section, the solutions $\sigma_{nn}^{(k)}$ of derived models are tested against numerical results.¹⁴ For demonstration purposes, only cubic elastic materials are chosen for comparison (see Appendix D for the corresponding elastic properties).

Following the derived expressions, Eqs. (14), (21) and (24), the mean value $\langle \sigma_{nn} \rangle$ and standard deviation $s(\sigma_{nn})$ of PDF(σ_{nn}) should depend trivially on the external loading Σ^{lab} . Using suggested normalization, $\langle \sigma_{nn} \rangle / \text{tr}(\Sigma^{\text{lab}})$ and $s(\sigma_{nn}) / \Sigma_{\text{mis}}^{\text{lab}}$, the first two statistical moments become independent of Σ^{lab} , which is demonstrated in Fig. 7 for 27 different loading configurations. Very good agreement¹⁵ between the prediction and numerical results confirms the validity of the derived expressions being of the form $\sigma_{nn}^{(k)} = A^{(k)}\Sigma_{zz} + B^{(k)}(\Sigma_{xx} + \Sigma_{yy})$ for any k . Hence, a tensile loading Σ will be used hereafter without the loss of generality.

In Fig. 8 the normalized standard deviation $s(\sigma_{nn})/\Sigma$ is shown for polycrystalline Li (cubic symmetry) as a function of effective GB stiffness parameter E_{12} , which is a single characteristic parameter of the $[abc]$ - $[def]$ GB. Results of different models from Table 2 are compared with the results of finite element simulations. The Li is chosen because of very high elastic anisotropy ($A^u = 7.97$), which makes the comparison more challenging.

Although none of model predictions for $s(\sigma_{nn})/\Sigma$ are very accurate, some of the models are more appropriate than others. The $L_n - L_t$ -chain (full version) model results are grouped into three families (with a given color) with a common axial chain length $L_n = 0, 2$ or 5 . While the response of the $L_n = 0$ (red) family is too steep for all transverse chain lengths L_t , overestimating the $s(\sigma_{nn})/\Sigma$ at large E_{12} ,

¹⁴ Having the exact constitutive (Hooke's) law, there are practically no physical uncertainties in numerical simulations besides finite size effects, which can be diminished by using sufficiently large aggregates and sufficiently dense finite element meshes.

¹⁵ Observed deviations from 1/3 in Fig. 7(a) are due to numerical artifacts which result from the division of two small numbers, $\langle \sigma_{nn} \rangle / \text{tr}(\Sigma^{\text{lab}})$, and the fact that $\langle \sigma_{nn} \rangle$ is approximate.

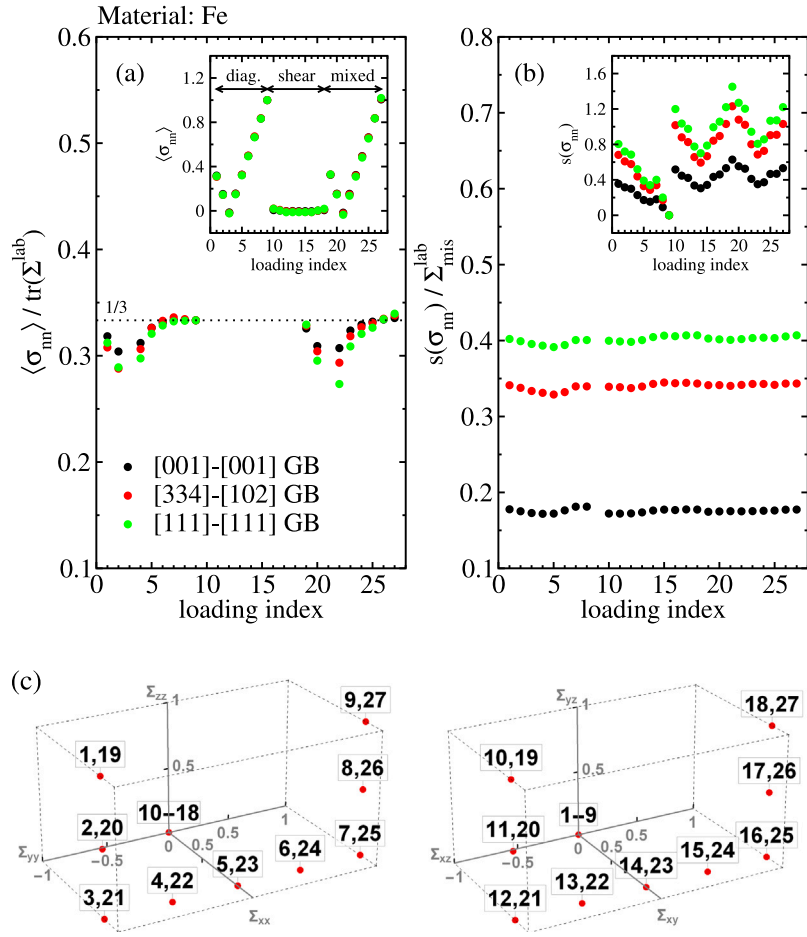


Fig. 7. Effect of external loading can be decoupled from other influences by a suitable choice of normalization factor (a) $\text{tr}(\Sigma^{\text{lab}})$ for mean value $\langle \sigma_{nm} \rangle$ and (b) $\Sigma_{\text{mis}}^{\text{lab}}$ for standard deviation $s(\sigma_{nm})$. Simulation results are shown for Fe, 27 different external loadings Σ^{lab} and three GB types. Non-normalized values are shown in the insets (a) and (b). Panel (c) shows correspondence between Σ^{lab} and loading index (1 – 27).

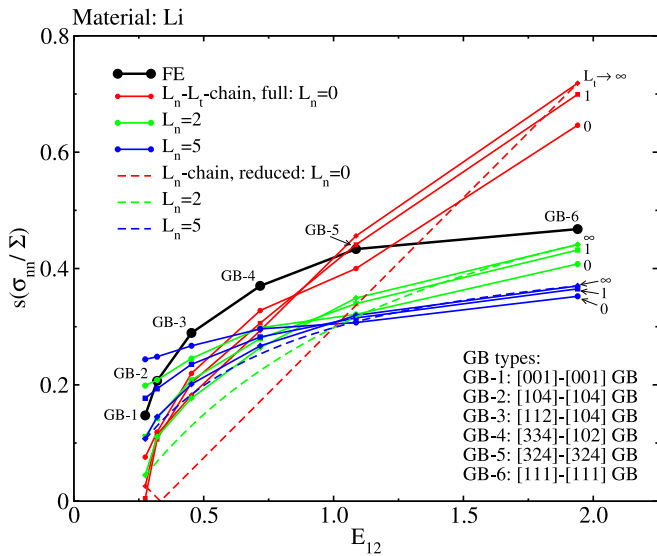


Fig. 8. Standard deviation $s(\sigma_{nm}/\Sigma)$ as a function of effective GB-stiffness parameter E_{12} . A comparison is shown between numerical results (FE) and different model predictions from Table 2. The results are evaluated for Li on all GBs of a specific type, and thus corresponding to a certain E_{12} value. Six GB types are used in total (here, solid lines are unphysical and are meant only to indicate the trend).

the response of $L_n = 2$ (green) and $L_n = 5$ (blue) families is too gradual for $L_t \lesssim 2$, overestimating the $s(\sigma_{nm}/\Sigma)$ at small E_{12} . These models are recognized as inappropriate. In addition, all three model families show, for $L_t = 0$, a sudden change in the slope of $s(\sigma_{nm}/\Sigma)$, which is not observed numerically, suggesting that $L_t = 0$ models are also unsuitable. Most favorable are therefore $2 \lesssim L_n \lesssim 5$, $L_t \gtrsim 1$ models, which predict $s(\sigma_{nm}/\Sigma)$ consistently below the numerical curve. This systematic underestimation of fluctuations is compensated later in Section 3.4.2 by accounting for loading fluctuations, which are generated by external loading mediated through the anisotropic bulk surrounding the $L_n - L_t$ -chain model (see last stage in Fig. 4).

In Fig. 8 also the results of the L_n -chain (reduced version) model are shown for comparison. The advantage of the latter is the compact formulation of the $\sigma_{nm}^{(2)}$ and its statistical moments. The resulting $s(\sigma_{nm}/\Sigma)$ curves show similar dependence of E_{12} as the corresponding $L_n - L_t \rightarrow \infty$ (full version) models, however, with slightly reduced fluctuations in the mid- E_{12} range.¹⁶ Since in either case additional fluctuations need to be added to fit the numerical results, also the validity of the L_n -chain model, with $2 \lesssim L_n \lesssim 5$, is considered appropriate.

In Fig. 9 a response of a single [112]-[112]- $\Delta\omega$ GB type is shown in terms of $s(\sigma_{nm}/\Sigma)$ as a function of $\Delta\omega$, using numerical simulations and model predictions from Table 2 for a polycrystalline Li to associate

¹⁶ Since the responses on [001]-[001] GB type (with corresponding $E_{12,\text{min}}$) and [111]-[111] GB type (with corresponding $E_{12,\text{max}}$) are independent of twist angles ω_1, ω_2 , the predictions of the L_n -chain model (reduced version) and $L_n - L_t$ -chain model (full version, with $L_t \rightarrow \infty$) are the same.

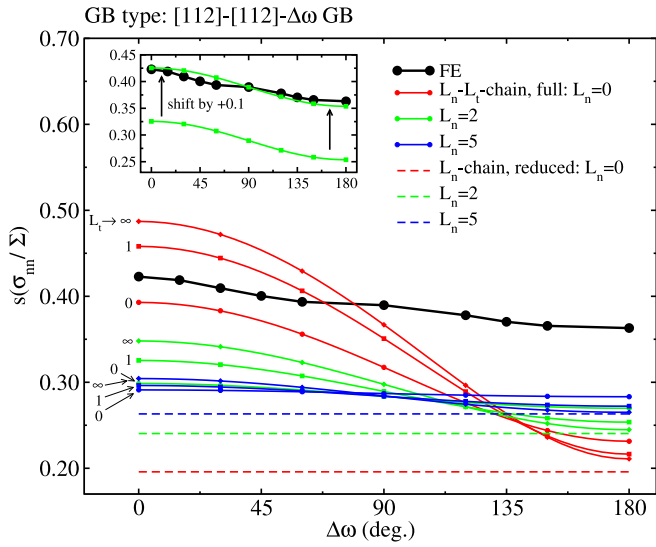


Fig. 9. Standard deviation $s(\sigma_{nn}/\Sigma)$ as a function of twist-angle difference $\Delta\omega$ associated with the [112]-[112]- $\Delta\omega$ GB type. A comparison is shown between numerical results (FE) and different model predictions from Table 2. The properties of Li are used. Note that [112]-[112]- $\Delta\omega$ GBs correspond to $E_{12} = 0.77$, irrespective of the value of $\Delta\omega$. Inset shows the agreement between the FE result and the response of $L_n - L_t$ -chain model for $L_n = 2$ and $L_t = 1$ (note the artificial shift accounting for the missing fluctuations).

with results of Fig. 8. According to the numerical curve, very small variations in $s(\sigma_{nn}/\Sigma)$ are observed across the whole $\Delta\omega$ range, which is consistent with previous results (El Shawish et al., 2021). Using the same coloring and labeling scheme as in Fig. 8, a very good agreement with simulations is achieved for the $L_n - L_t$ -chain model for $L_n = 2$ and $L_t = 1$ (see the inset of Fig. 9). The other two families of curves produce either too big ($L_n = 0$, in red) or too small ($L_n = 5$, in blue) variations across the $\Delta\omega$ range. Since the twist angle degrees of freedom are integrated out, the response of the L_n -chain (reduced version) model is independent of $\Delta\omega$, which is, by design, also in good agreement with numerical results.

Results of Figs. 8 and 9 seem to favor the $L_n - L_t$ -chain model with $L_n \sim 2$ and $L_t \sim 1$. This is further corroborated by noting that the overall shift in $s(\sigma_{nn}/\Sigma)$ (by ~ 0.1), used to fit the simulation results in the inset of Fig. 9, is matching very well the gap at $E_{12} = 0.77$ (corresponding to [112]-[112]- $\Delta\omega$ GB) between the two corresponding curves in Fig. 8.

In the following, the evaluation of derived models is shifted from macro- to mesoscale using a linear correlation property, $\sigma_{nn}^{(k)}/\Sigma = \alpha^{(k)} + \beta^{(k)} \cos^2 \theta$, derived for the external uniaxial loading Σ .¹⁷ Statistical analysis employed on a subset of GBs with a fixed angle θ (or $\cos^2 \theta$) between the GB normal and uniaxial loading direction is useful because it allows one to test the validity of individual parts of expressions in $\sigma_{nn}^{(k)}$ (e.g., $\alpha^{(k)}$ and $\beta^{(k)}$). Such analyses are demonstrated in Figs. 10 and 11 for polycrystalline Li.

The local mean $\langle \sigma_{nn}/\Sigma \rangle$ and standard deviation¹⁸ $s(\sigma_{nn}/\Sigma)$ are shown in Fig. 10 as a function of $\cos^2 \theta$. Due to finite aggregate size, the mean and standard deviation are obtained at given $\cos^2 \theta$ by averaging over Euler angles ψ and ϕ on a finite (but small) range of GB tilt angles $\delta(\cos \theta) = 0.05$. The proposed linear trend is nicely reproduced, showing a clear effect of different GB types on the corresponding slopes K of fitted lines. In general, slope K increases with increasing GB stiffness

(parameter E_{12} , see also Fig. 11). However, there is a very weak effect of $\Delta\omega$ on the corresponding slope K when evaluated on the [112]-[112]- $\Delta\omega$ GB. This suggests that, on average, the GB stiffness (which is independent of $\Delta\omega$, see Eq. (B.2)) is the main contributor to σ_{nn} at given $\cos^2 \theta$.

It is interesting to note a crossing point in Fig. 10(a) at $\cos^2 \theta = 1/3$ at which σ_{nn} becomes independent of both material and GB type properties. This point is exactly reproduced by all non-trivial models ($\sigma_{nn}^{(k)}, k > 0$). The value of σ_{nn} at this point is $\Sigma/3$ (actually $\text{tr}(\Sigma)/3$ for arbitrary loading).

The simulation results from Fig. 10(a) are analyzed further in Fig. 11 where the actual dependence of slope K with E_{12} is presented and compared with predictions of the models from Table 2. While the increasing trend is captured well by all the models, none of the presented curves fit the numerical result very accurately for all E_{12} . Actually, this holds true for any combination of L_n, L_t values in the $L_n - L_t$ -chain model. The most suitable solution is chosen to be that of the L_n -chain model (reduced version) for $L_n = 2$, which matches the true K values at the two extreme E_{12} points. The same agreement is observed also for other cubic materials (not shown).

The $L_n - L_t$ -chain model with $L_n \sim 2$ and $L_t \sim 1$, which has been selected as the most suitable model at the macroscale (see Figs. 8 and 9), provides in Fig. 11 a very similar $K(E_{12})$ response as the L_n -chain model for $L_n = 2$. In this sense, both models seem equally well acceptable, however, the latter one will be preferred due to much more compact formulation.

In summary, although the qualitative behavior of σ_{nn} is well reproduced by the selected model ($\sigma_{nn}^{(2)}$ for $L_n \sim 2$) on a wide range of parameters (associated with external loading, material properties and GB type), two ingredients still seem to be missing. The first one is related to the systematic shortage of stress fluctuations observed on the macroscale and the second one is linked to the insufficient agreement of mean stresses on the mesoscale. Both issues are addressed in the next section.

3.4. Model upgrades

3.4.1. Variable axial strain constraint and 3D effects

The observed inconsistency in Fig. 11 is attributed to the (i) imposed axial strain constraint of the L_n -chain model and (ii) 3D effects which have been omitted in the model derivation. The 3D effects include primarily a non-zero lateral coupling of the axial grain chain with the elastic bulk. Depending on the relative axial stiffness of the chain with respect to the bulk, this coupling may effectively either increase or decrease the chain stiffness, resulting in larger or lower σ_{nn} , respectively. To model this in 1D framework, the elastic properties of both GB grains and buffer grain need to be amended.¹⁹ Regarding the GB grains, therefore

$$E_{12} \rightarrow E_{12} + \delta E_{12}, \quad (30)$$

$$\delta E_{12} = \mathcal{F}(E_{12}, v_{12}, L_n, A^u),$$

and similarly

$$v_{12} \rightarrow v_{12} + \delta v_{12}, \quad (31)$$

$$\delta v_{12} = \mathcal{F}(E_{12}, v_{12}, L_n, A^u).$$

The assumed functional dependence of δE_{12} in Eq. (30) can be explained with the help of Fig. 12 where the field lines are used to

¹⁷ For cubic lattices and $E_3 = 1$, $\alpha^{(2)} = (1 - E_{12})/(2 + L_n E_{12})$ and $\beta^{(2)} = 1 + 3(E_{12} - 1)/(2 + L_n E_{12})$.

¹⁸ The $s(\sigma_{nn}/\Sigma)$ results from Fig. 10(b) are discussed latter in Section 3.4.2.

¹⁹ Alternatively, one could try to resolve the observed inconsistency by simply assuming a variable buffer length $L_n = \mathcal{F}(E_{12}, A^u)$. However, it becomes clear from Fig. 11 that such an approach fails to produce correct slopes K for $E_{12} \sim 1$ (as there is no effect of L_n for $E_{12} = E_3 = 1$). This confirms that the observed mismatch cannot be resolved solely by assuming a variable axial strain constraint, controlled by L_n in Eq. (11), and that 3D effects need to be employed on E_{12} and v_{12} , too.

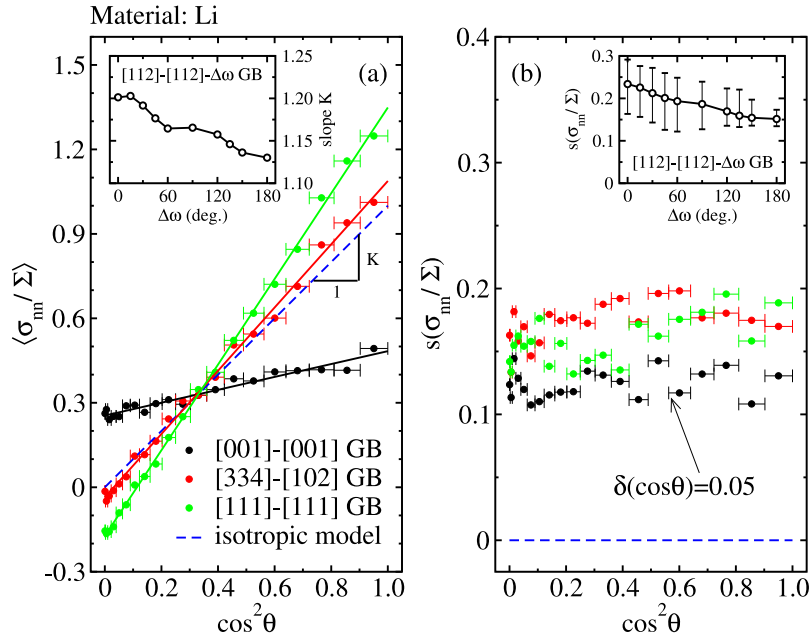


Fig. 10. (a) Mean local stress $\langle \sigma_{nn} / \Sigma \rangle$ and (b) corresponding standard deviation $s(\sigma_{nn} / \Sigma)$, both evaluated numerically as a function of $\cos^2 \theta$ for a finite range of GB tilt angles, $\delta(\cos \theta) = 0.05$. The averaging range is denoted by horizontal error bars and the averaged values by dots. Lines in panel (a) are linear fits with slope K . Twist angle difference $\Delta\omega$ in [112]-[112]- $\Delta\omega$ GB has a negligible influence on slope K (inset (a)) but a significant effect on the standard deviation (inset (b)).

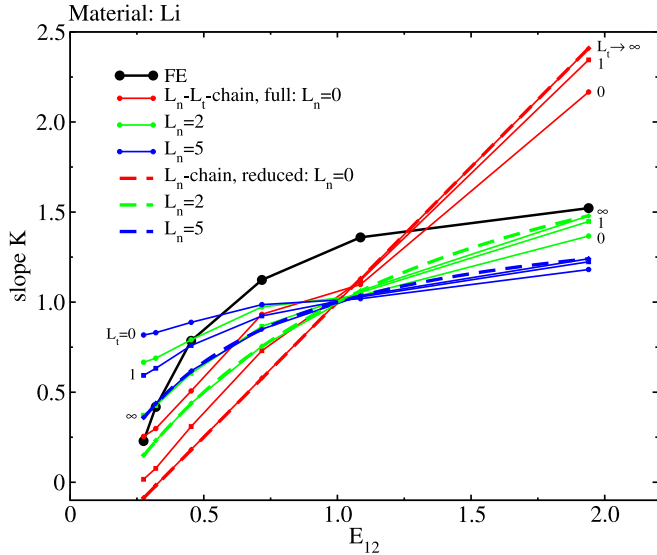


Fig. 11. Slope K , obtained from Fig. 10(a), versus effective GB-stiffness parameter E_{12} . A comparison is shown between numerical results (FE) and different model predictions from Table 2. The properties of Li are used. Note that L_n -chain model (reduced version) and L_n-L_t -chain model (full version with $L_t \rightarrow \infty$) provide identical slopes $K = 1 + 3(E_{12} - 1)/(2 + L_n E_{12})$, assuming $E_3 = 1$. There is no effect of L_n when $E_{12} = E_3 = 1$.

visualize schematically the force field around the two GB grains under tensile loading. While force lines are always parallel in the 1D model (no lateral coupling with the bulk), they concentrate within/outside the stiffer/softer (larger/smaller E_{12}) GB grains in the 3D model. Obviously, the effect gets stronger for $E_{12} \rightarrow E_{12,\max}$ or $E_{12} \rightarrow E_{12,\min}$ and for increasing material anisotropy A^u . To account for more (less) field lines in stiffer (softer) GB grains, $\delta E_{12} > 0$ ($\delta E_{12} < 0$) should be used in 1D modeling. However, using a non-zero δE_{12} (or δv_{12}) affects also the boundary condition applied on the chain scale in Eq. (11). Since the

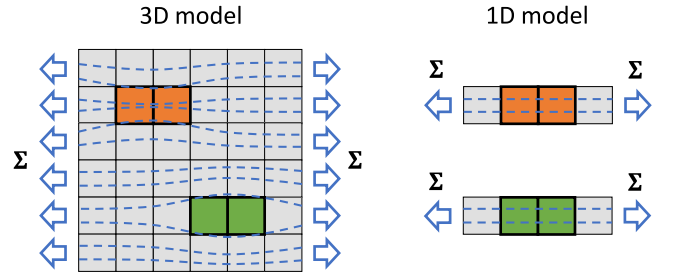


Fig. 12. Schematic view of field lines crossing through the stiff (orange) and soft (green) GB grains in 3D and 1D models. (For interpretation of the references to color in this figure legend, the reader is referred to the web version of this article.)

latter is regulated also by the length of the buffer grain L_n , both δE_{12} and L_n are coupled as indicated in Eq. (30).

In a similar way, the properties of the buffer grain (of length L_n) are modified due to lateral coupling with the bulk

$$\begin{aligned} E_3 &\rightarrow E_3 + \delta E_3 \approx 1, \\ v_b &\rightarrow v_b + \delta v_b \approx \langle v \rangle. \end{aligned} \quad (32)$$

The above mapping follows from the fact that a chain of randomly oriented grains, when coupled laterally to the bulk, should, on average, behave similarly as the bulk itself. An equality in Eq. (32) is achieved for $L_n \rightarrow \infty$, while very small deviations are observed at $L_n = 2$ (see footnote 21). As already mentioned, this modification has been already implemented in Eq. (22) by setting $E_3 = 1$ and $v_b = \langle v \rangle$.

Since E_b and v_b can be evaluated (e.g., numerically) by Eqs. (23) for a given material and L_n , the corresponding increments can be estimated directly from Eqs. (32). By design, the same increments should also apply to GB grains, $(\delta E_{12}, \delta v_{12}) = (\delta E_3, \delta v_b)$, if $(E_{12}, v_{12}) = (E_3, v_b)$. Unfortunately, there seems to be no analytical approach to identify the increments for a general pair (E_{12}, v_{12}) . In the following, the functional dependence of δE_{12} (and δE_3) is therefore derived empirically for materials with cubic lattice symmetry, where further simplification is used due to mutual dependence of E_{12} and v_{12} ($v_{12} = \langle v \rangle + (E_{12}^{-1} - 1)/2$).

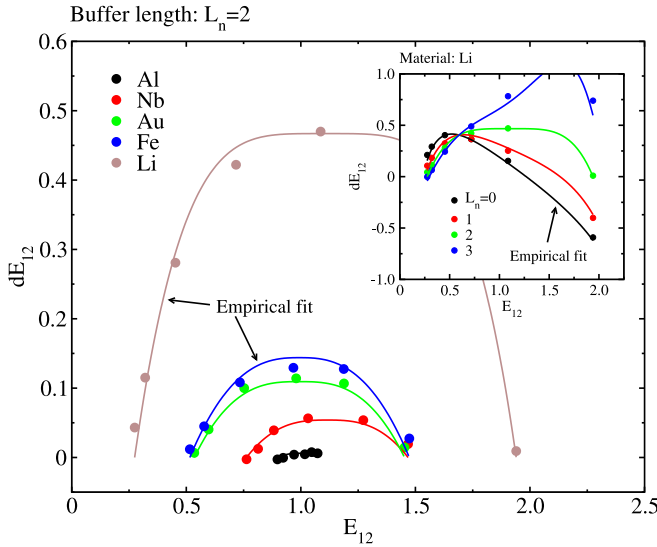


Fig. 13. Calculated (dots) and fitted (lines) increments δE_{12} as a function of E_{12} for the chosen reduced L_n -chain model (with $L_n = 2$) applied to various materials with cubic lattice symmetry. Fitting function, Eq. (36), has been chosen based on the observed symmetry $\delta E_{12}(E_{12})$ for $L_n = 2$. Inset shows that very good agreement is preserved also when the symmetric $L_n = 2$ fitting function is used for other L_n (shown for Li).

The expression for the reduced version of the L_n -chain model, Eq. (22), simplifies for cubic materials and general macroscopic loading to

$$\sigma_{nn}^{(2)} = \frac{2 + L_n}{2E_{12}^{-1} + L_n E_3^{-1}} \Sigma_{zz} + \frac{1}{2} \left(1 - \frac{2 + L_n}{2E_{12}^{-1} + L_n E_3^{-1}} \right) (\Sigma_{xx} + \Sigma_{yy}), \quad (33)$$

which reduces further for uniaxial macroscopic loading Σ as

$$\sigma_{nn}^{(2)}/\Sigma = \frac{1}{2} \left(1 - \frac{2 + L_n}{2E_{12}^{-1} + L_n E_3^{-1}} \right) + \frac{3}{2} \left(-\frac{1}{3} + \frac{2 + L_n}{2E_{12}^{-1} + L_n E_3^{-1}} \right) \cos^2 \theta, \quad (34)$$

where θ is an angle between the GB normal and uniaxial loading direction. As discussed before, the model can be upgraded by assuming $\delta E_{12} = \mathcal{F}(E_{12}, L_n, A^u)$ for the two GB grains and $\delta E_3 = \mathcal{F}(E_3, L_n, A^u)$ for the buffer grain. Both increments can be calculated numerically from the requirement that the resulting modified slope (a factor in front of $\cos^2 \theta$),

$$K = \frac{3}{2} \left(-\frac{1}{3} + \frac{2 + L_n}{2(E_{12} + \delta E_{12})^{-1} + L_n(E_3 + \delta E_3)^{-1}} \right), \quad (35)$$

is matching the corresponding K^{FE} slope obtained from the FE simulations for different E_{12} values and materials (see Fig. 11 where the results for Li are shown).²⁰

The results for δE_{12} are shown in Fig. 13 for $L_n = 2$ and various materials.²¹ As anticipated, δE_{12} depends strongly on the GB stiffness E_{12} , elastic grain anisotropy A^u and buffer length L_n (inset of Fig. 13). Interestingly, for $L_n = 2$ a (quasi) symmetry is recognized in $\delta E_{12}(E_{12})$

²⁰ The corresponding increments are deduced in two steps. First, δE_3 is identified from $K(E_{12} = E_3, E_3) = K^{\text{FE}}(E_3)$ for the assumed $E_{12} = E_3$ and $\delta E_{12} = \delta E_3$ in Eq. (35), where E_3 is evaluated numerically using Eq. (23) for a given material A^u and buffer length L_n . In practice, the $K^{\text{FE}}(E_3)$ value is estimated by interpolating from several $K^{\text{FE}}(E_{12})$ values. Once δE_3 is known, δE_{12} is obtained from $K(E_{12}, E_3) = K^{\text{FE}}(E_{12})$.

²¹ Results also show that the relative buffer stiffness, when coupled to the bulk, is bounded by $1 \leq E_3 + \delta E_3 \leq 1.03$ for $L_n \geq 2$ and all the materials shown in Fig. 13.

curves for all investigated materials.²² The symmetry is lost when $L_n \neq 2$.

Based on the observed symmetry in Fig. 13 for $L_n = 2$, the following empirical fit is proposed for all cubic materials with corresponding elastic anisotropy index A^u

$$\delta E_{12} = C_1 - |E_{12} - \bar{E}_{12}|^{C_2},$$

$$\bar{E}_{12} = \frac{1}{2} (E_{12,\text{min}} + E_{12,\text{max}}), \quad (36)$$

$$\delta E_{12}(E_{12,\text{min}}) = 0,$$

$$\delta E_{12}(E_{12,\text{max}}) = 0.$$

The best agreement with FE results is obtained for

$$C_1 = 0.08(A^u)^{0.85},$$

$$C_2 = \frac{\log C_1}{\log(E_{12,\text{max}} - E_{12,\text{min}}) - \log 2}. \quad (37)$$

It seems quite surprising that the proposed fitting function, Eq. (36), with only two adjustable parameters (0.08 and 0.85) in Eq. (37) provides such a good agreement for a wide range of (cubic) materials shown in Fig. 13. Good agreement remains also when the $L_n = 2$ fitting function is used for $L_n \neq 2$ models (assuming $E_3 + \delta E_3 = 1$ in Eq. (35)) as shown in the inset of Fig. 13. The identified empirical relation represents the second main result of this study.

3.4.2. Stochastic loading fluctuations

So far, the original external loading Σ^{lab} (also Σ) has been assigned to all GB models from Table 2. However, in reality, this assumption is true only on average. In fact, a GB and its immediate neighborhood far away from the external surfaces feel an external loading modified by fluctuations, $\Sigma + f$, where f stands for the fluctuation stress tensor. The fluctuations f arise as a consequence of bringing far-away loading Σ onto a GB neighborhood through the elastic bulk of anisotropic grains (see the last stage in Fig. 4).

To account for loading fluctuations in the estimation of σ_{nn} and PDF(σ_{nn}), it is assumed for simplicity that fluctuation normal stress f_{nn} is a random variable with Gaussian distribution $\mathcal{N}(0, s^2(f_{nn}))$, where the standard deviation depends on the external loading and on grain anisotropy, $s(f_{nn}) \approx \mathcal{F}(\Sigma, A^u)$. Dependence of $s(f_{nn})$ on internal GB degrees of freedom (e.g., θ , E_{12} , ω_1 , ω_2) is neglected to a first approximation, which is supported by the results of Fig. 10(b). The latter indeed show that standard deviation $s(\sigma_{nn}/\Sigma)$, evaluated on various $[abc]$ - $[def]$ GB types at fixed GB tilts $\cos^2 \theta$ with respect to external tensile loading Σ , is practically independent of $\cos^2 \theta$ (and thus of σ_{nn} itself), but slightly dependent on GB type.²³ Model of stress fluctuations is derived in Appendix E.

Considering that stress fluctuations are independent of stresses themselves, a new update can be proposed as

$$\begin{aligned} \bar{\sigma}_{nn}^{(k)} &= \sigma_{nn}^{(k)} + f_{nn}^{(k)}, \\ s^2(\bar{\sigma}_{nn}^{(k)}) &= s^2(\sigma_{nn}^{(k)}) + s^2(f_{nn}^{(k)}), \end{aligned} \quad (38)$$

$$\text{PDF}(\bar{\sigma}_{nn}^{(k)}) = (\text{PDF} \star \mathcal{N}(0, s^2(f_{nn}^{(k)}))) (\sigma_{nn}^{(k)}),$$

where symbol \star denotes a convolution.

To identify standard deviation $s(f_{nn}^{(k)})$ for tensile Σ , the results from Fig. 10(b) can be averaged over different GB tilts and shown in Fig. 14 for different materials as a function of A^u . Obtained standard deviation $s(f_{nn}/\Sigma)$ is set to be a measure of local stress fluctuations f_{nn} . As expected, $s(f_{nn}/\Sigma)$ increases with A^u following a simple empirical law $s(f_{nn}/\Sigma) = (0.070 \pm 0.018)(A^u)^{0.37 \pm 0.03}$. The \pm sign denotes a finite

²² The authors have not resolved yet whether the observed symmetry is a coincidence or an intrinsic property of the (reduced) L_n -chain model.

²³ While the primary source of fluctuations in Fig. 10(b) is the anisotropic GB neighborhood, the secondary source is a finite range of GB tilt angles, $\delta(\cos \theta) = 0.05$, which provides negligible contribution to $s(\sigma_{nn}/\Sigma)$.

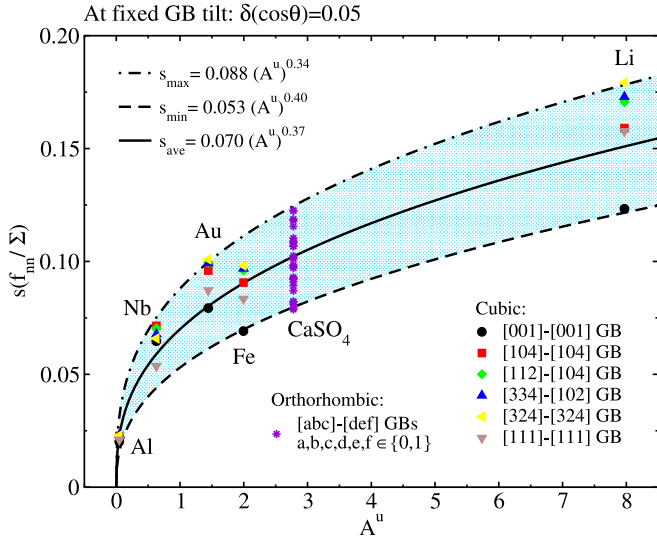


Fig. 14. Standard deviation of GB-stress (normal) fluctuations $s(f_m/\Sigma)$, evaluated numerically on different GB types with fixed GB tilt (and later averaged over different GB tilts, see Fig. 10(b)) and for different materials (A^u) under tensile loading Σ . A shaded region represents the proposed empirical domain of fluctuations. A generalization to arbitrary loading can be done by substituting Σ with Σ_{mis} on the vertical axis (see Appendix E).

width of $s(f_m/\Sigma)$ domain, which is attributed to GB internal degrees of freedom.

The empirical fit is generalized further to arbitrary loading using the familiar normalization for the second statistical moment (see Appendix E for more detail),

$$s(f_m) = \Sigma_{\text{mis}}(0.070 \pm 0.018)(A^u)^{0.37 \pm 0.03}. \quad (39)$$

The above relation applies not only to cubic but also to non-cubic materials.²⁴ For example, tensile fluctuations evaluated in calcium sulfate (CaSO_4), with orthorhombic lattice symmetry and $A^u = 2.78$, fit accurately within the proposed domain in Fig. 14.

4. Verification of upgraded models

4.1. Cubic materials

Statistical response PDF($\tilde{\sigma}_{nn}^{(2)}$) of the upgraded cubic GB model (using $L_n = 2$ and $E_3 + \delta E_3 = 1$ in Eq. (33)),

$$\tilde{\sigma}_{nn}^{(2)} = \frac{2}{(E_{12} + \delta E_{12})^{-1} + 1} \Sigma_{zz} + \frac{1}{2} \left(1 - \frac{2}{(E_{12} + \delta E_{12})^{-1} + 1} \right) (\Sigma_{xx} + \Sigma_{yy}) + f_{nn}, \quad (40)$$

where δE_{12} is estimated by Eqs. (36), (37) and $s(f_m)$ by Eq. (39), is verified in Fig. 15 for polycrystalline Fe under different macroscopic loadings Σ . The predicted PDF($\tilde{\sigma}_{nn}^{(2)}$) distributions are calculated numerically using Monte Carlo sampling of the two²⁵ Euler angles (θ, ψ), which are used to evaluate Σ_{xx} , Σ_{yy} and Σ_{zz} defined in Eq. (4). An excellent agreement with simulation results is demonstrated, confirming the accuracy of the proposed model for *arbitrary* GB type, *arbitrary* (cubic) material and *arbitrary* macroscopic loading conditions.

In Fig. 16 a comparison is shown for a polycrystalline Fe with elongated grains to verify the applicability of the derived models in

²⁴ It is also interesting to note that a hydrostatic loading Σ provides no GB stress fluctuations even in the case of anisotropic grains.

²⁵ Since $\sigma_{nn}^{(k)} = A^{(k)} \Sigma_{zz} + B^{(k)} (\Sigma_{xx} + \Sigma_{yy})$ for any k , the third Euler angle ϕ drops out from the $\sigma_{nn}^{(k)}$ expression.

materials with non-zero morphological texture (but with zero crystallographic texture). In this comparison, the PDF response is calculated on all GBs (random type) using the following simple relation (see Appendix F)

$$\text{PDF}_{\text{rnd}}(\tilde{\sigma}_{nn}^{(k)}) \approx \text{PDF}(\tilde{\sigma}_{nn}^{(0)}). \quad (41)$$

The response of random GBs is calculated using the convolution of the isotropic solution PDF($\sigma_{nn}^{(0)}$) and Gaussian distribution $\mathcal{N}(0, s^2(f_m))$ with $s(f_m)$ from Eq. (39).²⁶ The distributions are calculated numerically using Monte Carlo sampling of the two Euler angles (θ, ψ) with the following distribution functions (see Appendix G)

$$f(\cos \theta) = \frac{\lambda_z}{2} \left(\frac{1}{1 + (\lambda_z^2 - 1) \cos^2 \theta} \right)^{3/2}, \quad (42)$$

$$f(\psi) = \frac{1}{2\pi},$$

for $-1 \leq \cos \theta \leq 1$ and $0 \leq \psi \leq 2\pi$, with a scaling factor $\lambda_z > 0$ accounting for grain elongation along the Z -axis ($\lambda_z = 1$ denoting no scaling).

Again, an excellent agreement with simulation results is demonstrated in Fig. 16, which confirms the accuracy of the proposed model when applied to materials with *arbitrary* morphological texture.

In Fig. 17, the accuracy of GB models is furthermore tested on a local GB scale using FE simulations of a polycrystalline Li under tensile loading Σ as a reference. In particular, three models (of increasing complexity) are compared: (i) the isotropic model $\sigma_{nn}^{(0)}$, (ii) the reduced and upgraded version of the L_n -chain ($L_n = 2, L_t \rightarrow \infty$) model $\sigma_{nn}^{(2)}$ and (iii) the full version of the L_n - L_t -chain ($L_n = 2, L_t = 1$) model $\sigma_{nn}^{(3)}$. The accuracy of the models is tested locally by comparing $\sigma_{nn}^{(k)}$ values with FE results σ_{nn}^{FE} evaluated on individual GBs of particular type (three GB types are tested in total).

According to Fig. 17, both $\sigma_{nn}^{(2)}$ and $\sigma_{nn}^{(3)}$ models are comparable in accuracy, outperforming the simplest $\sigma_{nn}^{(0)}$ model on softer [001]-[001] and stiffer 111]-[111] GBs. The uncertainties (deviations from true FE values) in the $\sigma_{nn}^{(2)}$ model (and also $\sigma_{nn}^{(3)}$ model) are of Gaussian type with zero mean and standard deviation (exactly!) equal to $s(f_m)$ from Fig. 14 (see dashed lines in Fig. 17(b)). This confirms the validity (and consistency) of the $\sigma_{nn}^{(2)}$ model, which is shown to be accurate up to unknown loading fluctuations f_m (which are substantial in Li). The latter are therefore the only²⁷ source of local stress uncertainties (errors), $\sigma_{nn}^{(2)} - \sigma_{nn}^{\text{FE}} \approx f_m$, suggesting that $\tilde{\sigma}_{nn}^{(2)} \approx \sigma_{nn}^{\text{FE}}$.

4.2. Non-cubic materials

To provide accurate stress distributions for non-cubic materials, the evaluation of δE_{12} and δv_{12} would need to be derived (see Eqs. (30) and (31)) to account for variable axial strain constraint and 3D effects missing in the L_n -chain model. The procedure for that should follow the one described for cubic materials in Section 3.4.1. However, this is left for future analyses.

In Fig. 19 the simulation results for average stress $\langle \sigma_{nn} \rangle / \Sigma$ are presented which are evaluated on 190 [abc]-[def] GBs obtained as combinations of 19 planes defined in Fig. 18 for the orthorhombic material CaSO_4 under tensile loading Σ . For comparison, a smooth prediction of $\langle \sigma_{nn}^{(2)} \rangle / \Sigma$ from Eq. (24) is shown for arbitrarily chosen $L_n = 2$. A good qualitative agreement is demonstrated (without fine-tuning of L_n), implying that, to a good approximation, only two parameters, E_{12}

²⁶ Since the PDF of the FE model is calculated on all GBs of an aggregate, including those with smallest GB areas, the finite-size effects (due to poor meshing) result in wider PDF distributions. For this reason, a $\sim 40\%$ larger $s(f_m)$ is used in Fig. 16 to fit accurately the FE results.

²⁷ In case of an invalid GB model, standard deviation of local stress errors would be larger than that of loading stress fluctuations, $s(\sigma_{nn}^{(2)} - \sigma_{nn}^{\text{FE}}) > s(f_m)$.

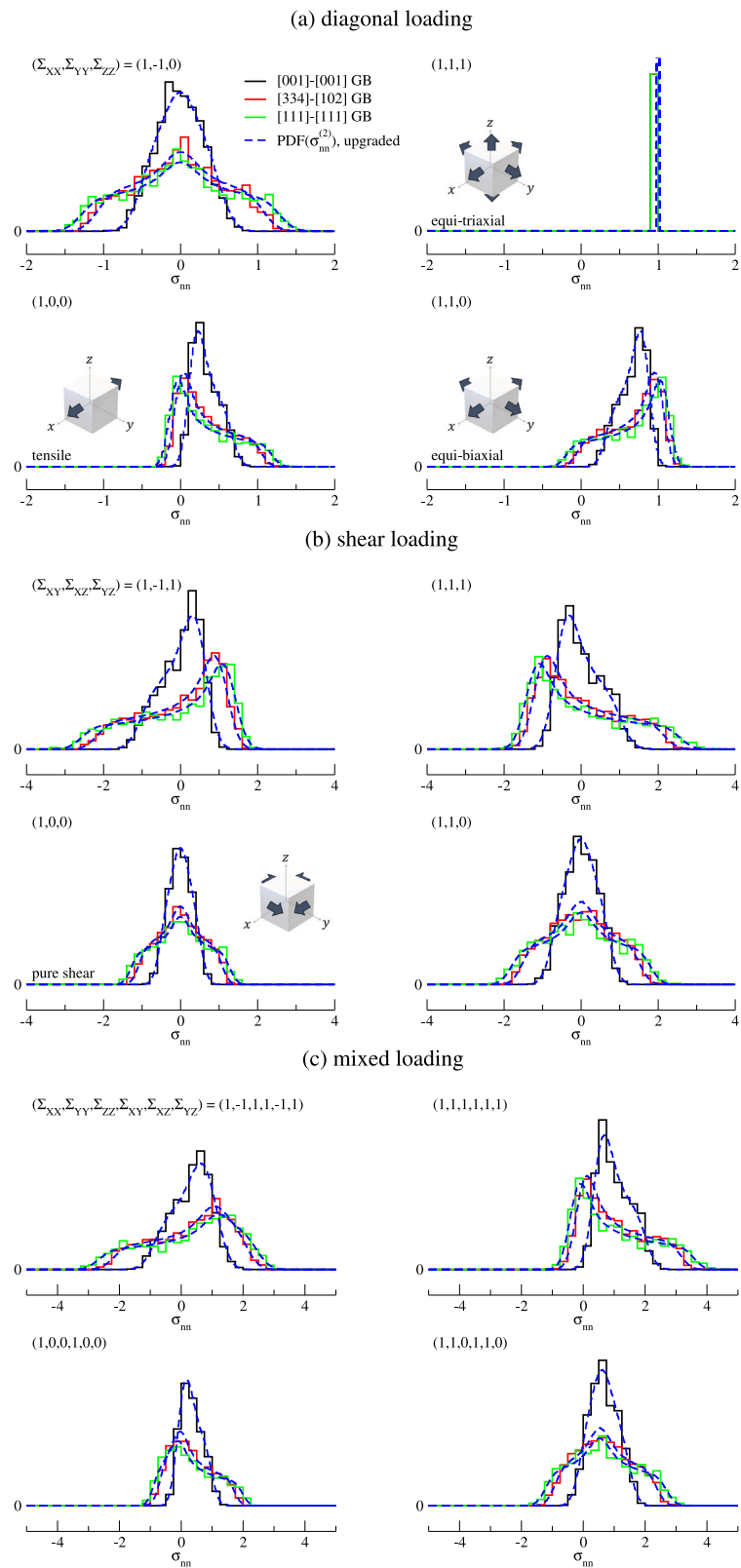


Fig. 15. Statistical stress distributions $PDF(\sigma_{mn})$ evaluated on three different GB types in Fe for 12 different macroscopic loadings (grouped into purely diagonal, purely shear and mixed loadings Σ). An excellent agreement is shown between simulation results (solid lines) and upgraded model predictions (dashed lines) for all the cases; cf. Eq. (40).

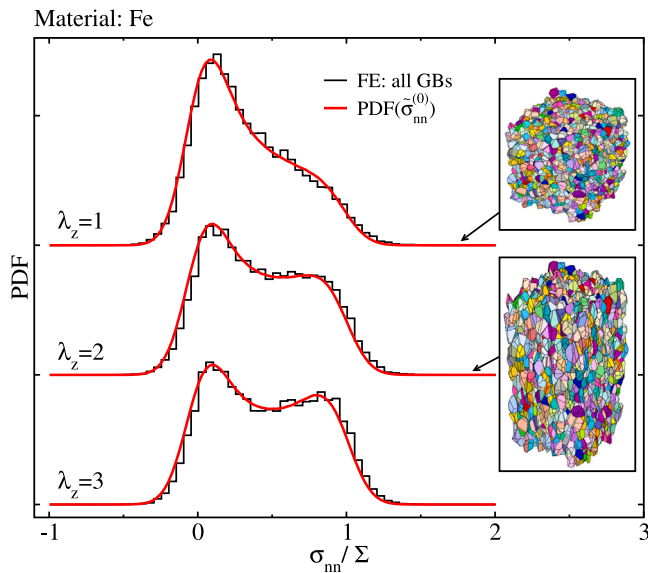


Fig. 16. Stress distributions $\text{PDF}(\sigma_{nm}/\Sigma)$ evaluated on all (random) GBs in Fe with grains elongated along the Z-axis (elongation factor λ_z) for tensile loading Σ along the X-axis. An excellent agreement is shown between simulation results (black) and model predictions (red) for all three cases; cf. Eqs. (41)–(42). (For interpretation of the references to color in this figure legend, the reader is referred to the web version of this article.)

and ν_{12} , are needed to characterize the response of a general GB, in agreement with the prediction of the GB model.

5. Discussion

5.1. Applications

The derived $\text{PDF}(\sigma_{nm})$ distributions are not only very accurate, as demonstrated for various scenarios (see Figs. 15 and 16), but also relatively undemanding in computational sense. If they are produced numerically, using Monte Carlo sampling for GB-normal directions, the results can be immediately used for several practical applications. For instance, we could predict the GB-damage initiation in complex geometries, using the probabilistic approach. If the GB strength σ_c of each GB type was known (or measured), and stress field $\Sigma(\mathbf{r})$ at position \mathbf{r} in the investigated component at least roughly estimated (e.g., in FE simulations, using homogeneous material), one can immediately obtain the probability of finding an overloaded GB (of a specific type) in a small volume $V(\mathbf{r})$ (with $\sim 10^3$ grains), $P(\mathbf{r}) = \int_{\sigma_c}^{\infty} \text{PDF}(\sigma_{nm}) d\sigma_{nm}$, using $\Sigma(\mathbf{r})$ as an input for external loading to produce $\text{PDF}(\sigma_{nm})$. If that probability exceeded the threshold value, $P(\mathbf{r}) > P_f$, a macroscopic-size crack may develop in volume $V(\mathbf{r})$, which might result in either controlled crack growth or even catastrophic failure of the component. With such approach, potentially dangerous regions, susceptible to intergranular cracking, can be quickly identified for any component and its loading. A more detailed analysis of such an application will be presented in a separate publication (El Shawish).

In all the examples presented so far, static elastic loads have been assumed in expressions for σ_{nm} and $\text{PDF}(\sigma_{nm})$. The procedure can be generalized also to dynamic stresses, provided that stress amplitudes remain in the elastic domain and inertia effects are negligible. In this respect, $\text{PDF}(\sigma_{nm})$ spectra can be used to predict even the initiation of GB-fatigue cracks (Koyama et al., 2015). Following the above procedure for static load and assuming time-dependent evolution of GB strength (due to the build-up of strain localization (Koyama et al., 2015)), the probability $P(\mathbf{r}, t) = \int_{\sigma_c(t)}^{\infty} \text{PDF}(\sigma_{nm}) d\sigma_{nm}$ becomes time dependent too. The measurement data can then be used, for example, to estimate how

P_f and GB-strength evolution $\sigma_c(t)$ change with the number of loading cycles.

5.2. Limitations

Although the semi-analytical σ_{nm} expression, derived for cubic crystal lattices, provides accurate $\text{PDF}(\sigma_{nm})$ distributions for a wide range of situations, it relies not only on analytical, but also on empirical considerations (estimation of δE_{12} and $s(f_{nm})$). A (quasi) symmetry of $\delta E_{12}(E_{12})$ curves was observed for $L_n = 2$ and all investigated materials. The origin of this feature is not yet understood, it might even be only accidental. Nonetheless, it can be very useful, since it allows us to make the search of the fitting function significantly simpler (Fig. 13). Due to that, it is important to gain a better understanding of this (quasi) symmetry for cubic lattices (and possibly even non-cubic lattices) in the future.

In a similar way, the effect of more distant grains has not been modeled explicitly. Instead it was conveniently packed into an empirical fit of $s(f_{nm})$, which represents the amplitude of GB-stress fluctuations (Fig. 14). The fact that these fluctuations are more or less independent of stresses, makes the fitting function $s(f_{nm})$ relatively simple and, most importantly, the calculation of $\text{PDF}(\sigma_{nm})$ very accurate (by applying Gaussian broadening with known width $s(f_{nm})$). However, the accuracy on a local GB scale is limited by the same $s(f_{nm})$ (representing the uncertainty of model predictions), and can be substantial in highly anisotropic materials. A possible improvement would necessarily include an exact modeling of the more distant grains (whose structure should probably be considered in a similar level of detail as the two GB grains). Unfortunately, this would probably result in very cumbersome and impractical solutions.

Moreover, since proposed analytical model (Fig. 5) is constructed upon the assumption of homogeneous stresses and strains within all the grains, GB-normal stresses are constant over the GBs, in contrast to the observed effects of geometric discontinuities (GB edges and GB triple junctions) in actual materials (or in FE simulations²⁸). In this sense, the predicted σ_{nm} (with uncertainty $s(f_{nm})$) should in fact represent accurately only the GB-normal stress in a central region of a realistic GB, i.e., away from all GB edges and GB triple junctions where stresses can be considerably larger or smaller. With such limitation, the proposed model for σ_{nm} is clearly not suitable for predicting individual GB-crack-initiation sites even for negligible effect of inhomogeneous neighborhood (in the $s(f_{nm}) \rightarrow 0$ limit). Instead, $\text{PDF}(\sigma_{nm})$ distribution, which is much less affected by GB-edge and GB-triple-junction effects, could be used in the probabilistic modeling to estimate the probability for GB-crack initiation in a reasonably large material volume ($\gtrsim 10^3$ grains, see Section 5.1).

5.3. Alternative approaches

The derivation of GB models was based on two major ideas: the perturbative approach and the Saint Venant's principle. A possible alternative approach could follow one of the well-known methods, used for calculation of the effective elastic constants of polycrystals from single-crystal and structure properties. For example, in the self-consistent method invented by Kröner (1958), an effective stress-strain relation is derived, taking into account the boundary conditions for stresses and strains at the GBs, which are only statistically correct. Analytical results are given for macroscopically isotropic polycrystals, composed of crystal grains with cubic symmetry (Hershey, 1954), and also for a general lattice symmetry (Kröner, 1958). Replicating such approach, the established relation between the local (single-grain) and

²⁸ In the FE analysis conducted here, the GB-edge and GB-triple-junction effects have been averaged out to obtain a single GB-normal-stress value σ_{nm}^{FE} for each GB of the FE model, see Appendix A.

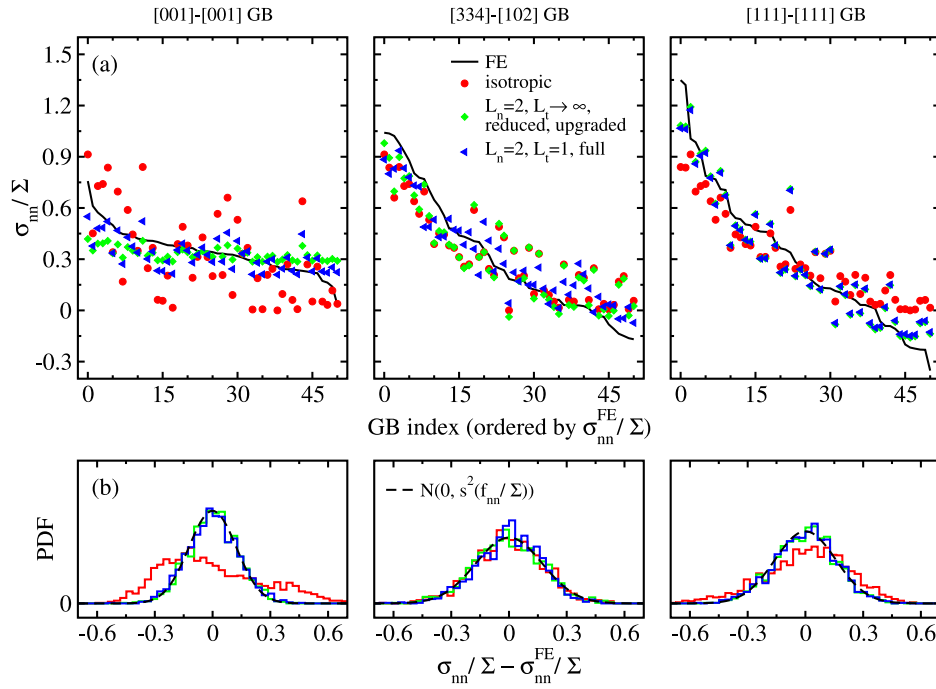


Fig. 17. (a) Local σ_{nn}/Σ stress response in Li under macroscopic tensile loading Σ . A comparison is shown between FE simulation (lines) and the results of three GB models (shapes). The 50 largest GBs in a 4000-grain aggregate (see Fig. 1) are shown, to which a specific GB type ([001]-[001], [334]-[102] or [111]-[111]) is assigned in each panel. The GBs are sorted (indexed) in descending order with respect to FE results for stresses. (b) Probability distributions (PDF) of discrepancy between the model prediction and FE result for GB stress, demonstrating how accurate the three GB models are (locally). All 1631 special GBs are considered in the PDF (as opposed to 50 shown in (a)). Gaussian distributions with standard deviations $s(f_m/\Sigma)$ from Fig. 14 are added for comparison (no fitting has been applied).

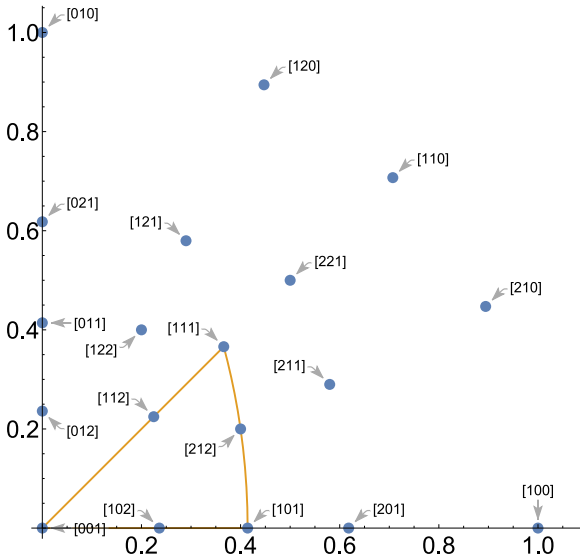


Fig. 18. 19 representative directions $[abc]$, from which GB normals in either GB grain were selected for orthorhombic material (CaSO_4). They correspond to 190 different GB types $[abc]-[def]$, considered in our numerical studies. The standard stereographic triangle is shown for reference.

macroscopic quantities would need to be modified to account for bi-crystal instead of single-crystal local quantities. While this might be worth trying, it has (at least) one significant shortcoming, common to all multi-scale techniques. It fails to reproduce additional degrees of freedom on a local scale (that would manifest themselves in stress fluctuations and thus in wider $\text{PDF}(\sigma_{nn})$ distributions), given there are fewer degrees of freedom on a macroscopic scale. Therefore, additional

improvements would be needed (as it was done here) to obtain accurate $\text{PDF}(\sigma_{nn})$. A detailed analysis along these lines is left for future work.

6. Conclusions

In this study, a perturbative model of grain-boundary-normal stresses has been derived for an arbitrary grain-boundary type within a general polycrystalline material, composed of randomly oriented elastic continuum grains with arbitrary lattice symmetry, and under a general uniform external loading. The constructed perturbative models have been solved under reasonable assumptions, needed to obtain compact, yet still accurate analytical and semi-analytical expressions for local grain-boundary-normal stresses and the corresponding statistical distributions. The strategy for deriving the models was based on two central concepts. Using the perturbation principle, the complexity of the model is gradually increased in each successive step, allowing us to first solve and understand simpler variants of the model. Following the Saint Venant's principle, anisotropic elastic properties of the two grains closest to grain boundary have been considered in full, while the effect of more distant grains has been modeled in much smaller detail, using average quantities such as elastic grain anisotropy or bulk isotropic stiffness parameter.

The following conclusions have been reached from the solutions of derived perturbative models:

- The general k th order solution for the local grain-boundary-normal stress is of the following form: $\bar{\sigma}_{nn}^{(k)} = A^{(k)}\Sigma_{zz} + B^{(k)}(\Sigma_{xx} + \Sigma_{yy}) + f_{nn}^{(k)}$, where $A^{(k)}$ and $B^{(k)}$ are the analytic functions of grain-boundary type and elastic material properties, Σ_{ii} is a diagonal component of the external loading tensor Σ , expressed in a local grain-boundary system, and $f_{nn}^{(k)}$ is a random variable, representing loading fluctuations.
- To a good approximation ($k = 2$), the response on a chosen grain boundary can be characterized by just two parameters: E_{12} measures the average stiffness of grain-boundary neighborhood along

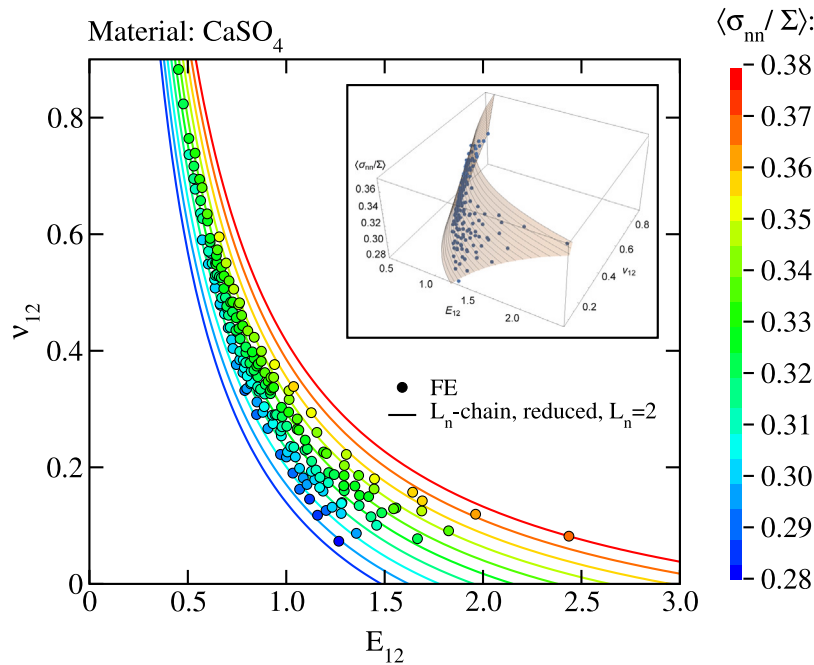


Fig. 19. Simulation results (circles) for $\langle \sigma_{nn} / \Sigma \rangle$ in CaSO_4 under tensile loading Σ , evaluated on 190 $[abc]-[def]$ GB types, constructed from the 19 selected directions shown in Fig. 18. For comparison, a smooth prediction (iso-lines) is shown for $\langle \sigma_{nn}^{(2)} / \Sigma \rangle$ of the $L_n = 2$ reduced model; cf. Eq. (24). The inset shows the same results in 3D plot.

the normal direction, while v_{12} is an effective Poisson's ratio, measuring the average ratio of transverse and axial responses in both adjacent grains.

- For an arbitrary lattice symmetry, $A^{(2)}$ and $B^{(2)}$ are simple functions, $\mathcal{F}(E_{12}, v_{12}, \langle E \rangle, \langle v \rangle, L_n)$, where $\langle E \rangle$ and $\langle v \rangle$ denote average elastic bulk properties, and $L_n \geq 0$ is a modeling parameter accounting for the amount of buffer grains. Also higher order solutions ($k > 2$) have been obtained, but with resulting expressions too cumbersome to be useful in practice.
- To account for 3D effects and realistic boundary conditions, a model upgrade has been proposed by assuming $E_{12} \rightarrow E_{12} + \delta E_{12}$ and $v_{12} \rightarrow v_{12} + \delta v_{12}$ in the expressions for $A^{(2)}$ and $B^{(2)}$, with δE_{12} and δv_{12} obtained from fitting the results of numerical simulations. A simple empirical relation for δE_{12} (and δv_{12}) has been derived for materials with cubic crystal lattices.
- To account for realistic stresses acting on a grain-boundary model, the external loading has been dressed by fluctuations, $\Sigma \rightarrow \Sigma + \mathbf{f}$. To a good approximation, the resulting fluctuations of grain-boundary-normal stresses (f_{nn}), have been found to be independent of stresses. Their distribution is Gaussian, with standard deviation of the form $s(f_{nn}) \approx \Sigma_{\text{mis}} \mathcal{F}(A^u)$, where $\mathcal{F}(A^u)$ is an empirical function, that increases with the value of universal elastic anisotropy index A^u .
- A comparison with finite element simulations has demonstrated that the derived semi-analytical expression for a local $\bar{\sigma}_{nn}^{(2)}$ is accurate only up to unknown stress fluctuations, i.e., the uncertainty of model prediction is $s(f_{nn})$. However, the corresponding statistical distributions, PDF($\bar{\sigma}_{nn}^{(2)}$), have been shown to be very accurate. Indeed, an *excellent agreement* with the simulation results has been found for arbitrary grain-boundary types in a general elastic untextured polycrystalline material²⁹ under arbitrary uniform loading.

²⁹ Materials with cubic lattice symmetry have been chosen in this article for demonstration purposes only.

- From the application point of view, a reliable tool has been derived for quick and accurate calculation of grain-boundary-normal-stress distributions. We expect its results should prove extremely useful for the probabilistic modeling of grain-boundary-damage initiation such as IGSCC.

CRediT authorship contribution statement

S. El Shawish: Conceptualization, Formal analysis, Investigation, Methodology, Visualization, Software, Writing – original draft. **T. Mede:** Investigation, Validation, Writing – review & editing.

Declaration of competing interest

The authors declare that they have no known competing financial interests or personal relationships that could have appeared to influence the work reported in this paper.

Data availability

Data will be made available on request.

Acknowledgments

We gratefully acknowledge financial support provided by Slovenian Research Agency (grant P2-0026). We also thank Jérémy Hure for useful discussions and comments that helped us to improve the manuscript.

Appendix A. Finite element aggregate model

Polycrystalline aggregate models are generated upon Voronoi tessellations (Quey et al., 2011) with periodic microstructures in all three spatial directions³⁰ (El Shawish et al., 2020). Finite element meshes

³⁰ Periodic boundary conditions imply the absence of free surfaces. Quantities derived in the model therefore correspond to bulk grains.

are generated with quadratic tetrahedral elements to preserve the geometry of the grains. An example of the model with 4000 grains, used throughout this study, is shown in Fig. 1(a). A general uniform loading Σ^{lab} is applied to the aggregate, where $\Sigma_{ij} = \langle \sigma_{ij} \rangle$ for averages taken over the entire volume of the aggregate model. Since grains are assumed ideally elastic, a unit loading can be applied, using a small strain approximation.

It is important to note that the analysis of each GB type requires a dedicated aggregate model. To isolate the effect of selected GB type, the same grain topology and finite element mesh (see Fig. 1(a)) are used in all of them.

Due to topological constraints, the same GB character cannot be assigned to all GBs. In practice, a chosen $[abc]-[def]-\Delta\omega$ GB type can be imposed on at most $\sim 17\%$ of GBs³¹ in a given aggregate, with remaining GBs belonging to a random type (*i.e.*, the two grains adjacent to the GB are assigned random orientations).

Also, it has been verified that the aggregate size (4000 grains) and finite element mesh density (~ 5 million total elements) are sufficiently large to produce negligible finite size effects.

The constitutive equations of the generalized Hooke's law are solved with finite element solver Abaqus (Simulia, 2016) in a small strain approximation. Numerically calculated stress fields σ_i are then used to obtain a single $\sigma_{nn}(k)$ value for each GB k of a given type $[abc]-[def]-\Delta\omega$. In short, $\sigma_{nn}(k)$ is calculated by projecting stress σ_i onto a GB normal $n^{(k)}$ and averaging over all finite elements i touching the GB k ; $\sigma_{nn}(k) = \sum_i A_i^{(k)} n^{(k)} \cdot \sigma_i \cdot n^{(k)} / \sum_i A_i^{(k)}$, where $A_i^{(k)}$ is the area of GB-element facet touching the GB, and $\sigma_i = 1/3 \sum_{j=1}^3 \sigma_{i,j}$ is Cauchy stress averaged over three Gauss points j of element i , that are located closest to the GB plane. Besides local stresses, the first two statistical moments, the mean value and standard deviation of PDF(σ_{nn}), are calculated as $\langle \sigma_{nn} \rangle = \sum_k A_k \sigma_{nn}(k) / \sum_k A_k$ and $s(\sigma_{nn}) = \sqrt{\langle \sigma_{nn}^2 \rangle - \langle \sigma_{nn} \rangle^2}$, respectively, for A_k denoting the area of GB k . The summation k is performed over all special GBs of a given type.³²

Appendix B. Analytic expressions for grains with cubic lattice symmetry

In this section, analytic expressions for cubic lattice symmetry are given for completeness. It is assumed that rotation \mathbf{R}^{cry} , defined in Eq. (1), is used for expressing the crystallographic properties of the grain in a local GB coordinate system, whose GB-plane normal (local z -axis) is oriented along the $[hkl]$ direction of the grain (crystallographic) coordinate system and with ω denoting the twist angle about the GB normal.

Strain component in the direction of GB normal can be expressed (for a cubic grain) as (see Eq. (B.1) in Box II) where $S_{11} := s_{1111}^{\text{cry}}$, $S_{12} := s_{1122}^{\text{cry}}$ and $S_{44} := 4 s_{2323}^{\text{cry}}$ are the components of compliance tensor of a grain in Voigt notation and $S_0 := S_{11} - S_{12} - S_{44}/2$. Expressions for the other two diagonal components of strain tensor, ϵ_{xx} and ϵ_{yy} , are derived analogously, but are omitted here for brevity.

The effective GB-stiffness parameter E_{12} , measuring the average stiffness of GB neighborhood along the GB-normal direction, takes the following form (for cubic grains)

$$E_{12} = \frac{2 \langle E \rangle^{-1}}{s_{3333}^{\text{GB,abc}} + s_{3333}^{\text{GB,def}}} = \frac{\langle E \rangle^{-1}}{S_{11} - S_0 \left(\frac{(ab)^2 + (ac)^2 + (bc)^2}{(a^2 + b^2 + c^2)^2} + \frac{(de)^2 + (df)^2 + (ef)^2}{(d^2 + e^2 + f^2)^2} \right)}. \quad (\text{B.2})$$

³¹ Fraction $\sim 17\%$ denotes a ratio between the area of GBs of a selected GB type and the area of all GBs in the model. To improve statistical evaluations, GBs in the first category (special GBs) are selected from the largest available GBs in the aggregate. In a given aggregate with 4000 grains, the total number of GBs is 31154 and the number of special GBs is 1631.

³² The response of random GBs is calculated in an aggregate with randomly oriented grains and summation index k running over all GBs.

The effective GB Poisson's ratio ν_{12} , measuring the average ratio of transverse and axial responses (strains) in both GB grains, takes the following form (for cubic grains)

$$\nu_{12} = -\frac{\langle E \rangle}{4} \left(s_{3311}^{\text{GB,abc}} + s_{3322}^{\text{GB,abc}} + s_{3311}^{\text{GB,def}} + s_{3322}^{\text{GB,def}} \right) = \langle \nu \rangle + \frac{1}{2} (E_{12}^{-1} - 1), \quad (\text{B.3})$$

$$\text{where } \langle \nu \rangle = \frac{1}{2} (1 - \langle E \rangle (S_{11} + 2S_{12})).$$

Appendix C. General grain boundary model solution for cubic crystal lattices

The highest-order (reduced) solution $\sigma_{nn}^{(3)}$, derived in Section 3.2.6 for the most general grain-lattice symmetry and external loading, simplifies enormously for cubic lattice symmetry, where

$$\begin{aligned} s_{1111}^{\text{cry}} &= s_{2222}^{\text{cry}} = s_{3333}^{\text{cry}} := S_{11}, \\ s_{1122}^{\text{cry}} &= s_{1133}^{\text{cry}} = s_{2233}^{\text{cry}} := S_{12}, \end{aligned} \quad (\text{C.1})$$

and

$$\langle \nu \rangle = \frac{1}{2} (1 - (S_{11} + 2S_{12}) \langle E \rangle), \quad (\text{C.2})$$

which in turn implies

$$\begin{aligned} s_{il}^{hkl} &= -s_{ll}^{hkl} + (S_{11} + 2S_{12}), \\ s_{tt}^{hkl} &= \frac{1}{2} (s_{ll}^{hkl} + (S_{11} + 2S_{12})), \end{aligned} \quad (\text{C.3})$$

meaning $A_{\text{cub}}^{(3)}$ and $B_{\text{cub}}^{(3)}$ are only functions of Young's moduli E_{abc} and E_{def} along the GB-normal direction in both grains (see Eq. (C.4) in Box III). All the used quantities are dimensionless, with s' denoting

$$s' := \langle E \rangle (S_{11} + 2S_{12}) = 1 - 2 \langle \nu \rangle. \quad (\text{C.5})$$

E_{abc} and E_{def} appear only in combinations E_{12} and Δ_{12} , where

$$\Delta_{12} := \frac{4E_{abc}^{-1}E_{def}^{-1}}{(E_{abc}^{-1} + E_{def}^{-1})^2} - 1 = (E_{12} \langle E \rangle)^2 E_{abc}^{-1} E_{def}^{-1} - 1 \quad (\text{C.6})$$

is a sort of geometric mean of inverse Young's moduli of both grains, measuring the deviation from a single-grain scenario (*i.e.*, the $[abc]-[abc]$ GB type), in which Δ_{12} vanishes. If the effective GB stiffness E_{12} is a measure of the average stiffness of the $[abc]-[def]$ GB neighborhood along the GB-normal direction, then Δ_{12} represents an additional, orthogonal degree of freedom, that can break the σ_{nn} - and $s(\sigma_{nn})$ -degeneracies of GB types with the same E_{12} (but different values of Δ_{12}).

The GB-normal stress and the corresponding first two statistical moments thus become (see Eq. (C.7) in Box IV). The relevance of E_{12} parameter determining the $s(\sigma_{nn})$ for materials with cubic lattice symmetry was correctly identified already in El Shawish et al. (2021). The new parameter Δ_{12} in Eq. (C.7) represents a higher-order correction, which can, at least qualitatively, explain the (small) spread of $s(\sigma_{nn})$ values, observed numerically for GB types with the same E_{12} (see Fig. 13(a) in El Shawish et al. (2021)).

Appendix D. Material elastic properties

Elastic constants of single crystals with cubic symmetry, together with their aggregate properties, are listed in Table D.3 for several representative materials. The materials are ordered according to their universal elastic anisotropy index A^u (Ranganathan and Ostaja-Starzewski, 2008), where $A^u = 0$ corresponds to an isotropic crystal.

In Table D.4 the elastic constants of a single crystal with orthorhombic symmetry (CaSO_4) and its aggregate properties are gathered.

$$\begin{aligned}
\epsilon_{zz} &= \sum_{k,l=1}^3 s_{33kl}^{\text{GB}} \sigma_{kl} = \sum_{k,l,m,n,o,p=1}^3 R_{3m}^{\text{cry}} R_{3n}^{\text{cry}} R_{ko}^{\text{cry}} R_{lp}^{\text{cry}} s_{mnop}^{\text{cry}} \sigma_{kl} \\
&= \sigma_{xx} \left(\frac{S_0 \left(hk \left(2hk (h^2 + k^2 + l^2) \sin^2 \omega + l (k^2 - h^2) \sqrt{h^2 + k^2 + l^2} \sin 2\omega \right) + 2l^2 (h^2 k^2 + h^4 + k^4) \cos^2 \omega \right)}{(h^2 + k^2) (h^2 + k^2 + l^2)^2} + S_{12} \right) + \\
&+ \sigma_{yy} \left(\frac{S_0 \left(l \left(hk(h-k)(h+k) \sqrt{h^2 + k^2 + l^2} \sin 2\omega + 2l (h^2 k^2 + h^4 + k^4) \sin^2 \omega \right) + 2h^2 k^2 (h^2 + k^2 + l^2) \cos^2 \omega \right)}{(h^2 + k^2) (h^2 + k^2 + l^2)^2} + S_{12} \right) + \\
&+ \sigma_{zz} \left(\frac{S_0 (h^4 + k^4 + l^4)}{(h^2 + k^2 + l^2)^2} + S_{12} + \frac{S_{44}}{2} \right) + \\
&+ \sigma_{xy} \frac{2S_0 \left((h^2 k^2 (h^2 + k^2) - l^2 (h^4 + k^4)) \sin 2\omega + hkl (k^2 - h^2) \sqrt{h^2 + k^2 + l^2} \cos 2\omega \right)}{(h^2 + k^2) (h^2 + k^2 + l^2)^2} + \\
&+ \sigma_{xz} \frac{2S_0 \left(hk (k^2 - h^2) \sqrt{h^2 + k^2 + l^2} \sin \omega + l (-l^2 (h^2 + k^2) + h^4 + k^4) \cos \omega \right)}{\sqrt{h^2 + k^2} (h^2 + k^2 + l^2)^2} + \\
&+ \sigma_{yz} \frac{2S_0 \left(l (l^2 (h^2 + k^2) - h^4 - k^4) \sin \omega + hk (k^2 - h^2) \sqrt{h^2 + k^2 + l^2} \cos \omega \right)}{\sqrt{h^2 + k^2} (h^2 + k^2 + l^2)^2}, \tag{B.1}
\end{aligned}$$

Box II.

$$\begin{aligned}
A_{\text{cub}}^{(3)} &= \frac{(1 + (2L_t + s')E_{12})(L_n + 2s' + 4(L_t + s')E_{12}) + (2L_n L_t + L_n s' - 2s'^2)E_{12}) + (L_n + 2s')\Delta_{12}}{(1 + (2L_t + s')E_{12})(L_n + 2s' + 4(L_t + s') + (2L_n L_t + L_n s' - 2s'^2)E_{12}) + (L_n + 2s' + 4(L_t + s'))\Delta_{12}}, \\
B_{\text{cub}}^{(3)} &= \frac{1}{2} (1 - A_{\text{cub}}^{(3)}). \tag{C.4}
\end{aligned}$$

Box III.

$$\begin{aligned}
\sigma_{nn}^{(3)} &= A_{\text{cub}}^{(3)} \Sigma_{zz} + B_{\text{cub}}^{(3)} (\Sigma_{xx} + \Sigma_{yy}), \\
\langle \sigma_{nn}^{(3)} \rangle &= \frac{1}{3} \text{tr}(\Sigma^{\text{lab}}), \\
s(\sigma_{nn}^{(3)}) &= \frac{2\Sigma_{\text{mis}}^{\text{lab}}}{3\sqrt{5}} \left| \frac{(1 + (2L_t + s')E_{12})(L_n - 2L_t + 6(L_t + s')E_{12}) + (2L_n L_t + L_n s' - 2s'^2)E_{12}) + (L_n - 2L_t)\Delta_{12}}{(1 + (2L_t + s')E_{12})(L_n + 2s' + 4(L_t + s') + (2L_n L_t + L_n s' - 2s'^2)E_{12}) + (L_n + 2s' + 4(L_t + s'))\Delta_{12}} \right|. \tag{C.7}
\end{aligned}$$

Box IV.

Table D.3

Elastic constants C_{ij} (in Voigt notation) of single crystals with cubic symmetry (Bower, 2010) and their aggregate properties. C_{ij} and $\langle E \rangle$ are in units of GPa. Fe is assumed in gamma phase.

Crystal	C_{11}	C_{12}	C_{44}	$\langle E \rangle$	$\langle \nu \rangle$	A^u
Al	107.3	60.9	28.3	70.41	0.346	0.05
Nb	240.2	125.6	28.2	104.9	0.393	0.63
Au	192.9	163.8	41.5	79.40	0.424	1.44
Fe	197.5	125.0	122.0	195.2	0.282	2.00
Li	13.5	11.44	8.78	10.94	0.350	7.97

Appendix E. Model of stress fluctuations

The stress applied to the GB model (see, e.g., Fig. 5) is assumed to be equal to the external stress, modified by fluctuations, $\Sigma + \mathbf{f}(r)$, where $\mathbf{f}(r)$

is the fluctuation stress tensor at position r . In a large aggregate, where crystallographic orientations of the grains are uncorrelated with their shapes (assuming zero morphological texture), the average fluctuation stress tensor should go towards zero, i.e.,

$$\langle f_{ij}(r) \rangle_r = \langle (\mathbf{R}\mathbf{f}(r)\mathbf{R}^T)_{ij} \rangle_r = 0, \tag{E.1}$$

when averaged over all GBs of a chosen type (and thus having a specific value of E_{12} , ν_{12} , ...) and for a fixed GB-normal direction n (see Fig. E.20). This should be true in any coordinate system (\mathbf{R} denotes an arbitrary rotation matrix).

Since fluctuations are induced by external loading Σ and strain incompatibility of the grains (which correlates with the elastic anisotropy index A^u), it seems reasonable to assume that the corresponding standard deviation s depends on Σ and A^u , possibly on GB model intrinsic parameters (e.g., E_{12} , ν_{12} , ...), but not on the global aggregate (or external loading) rotation \mathbf{R} ,

$$s(f_{ij}(r)) = s(\mathbf{R}\mathbf{f}(r)\mathbf{R}^T)_{ij} = \mathcal{F}(\Sigma, A^u, E_{12}, \dots). \tag{E.2}$$

Table D.4

Elastic constants of a single crystal with orthorhombic symmetry (CaSO₄) (Simmons and Wang, 1971) and its aggregate properties. C_{ij} and $\langle E \rangle$ are in units of GPa.

Crystal	C_{11}	C_{22}	C_{33}	C_{12}	C_{13}	C_{23}	C_{44}	C_{55}	C_{66}	$\langle E \rangle$	$\langle \nu \rangle$	A^u
CaSO ₄	93.82	185.5	111.8	16.51	15.20	31.73	32.47	26.53	9.26	71.77	0.282	2.78

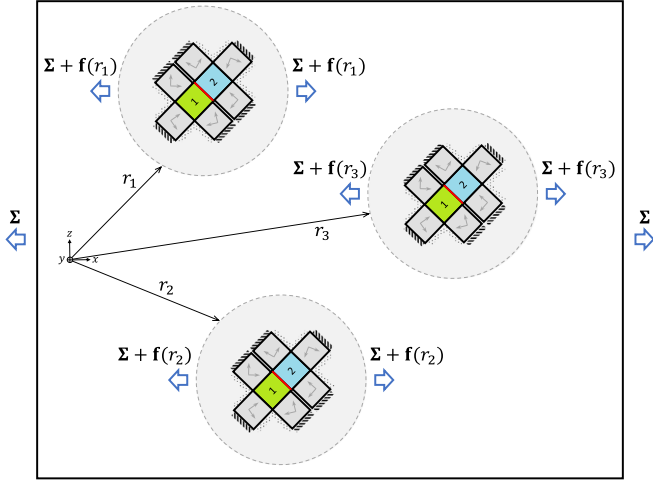


Fig. E.20. The fluctuation stress tensor $\mathbf{f}(r)$ at position r is defined as the difference between the actual loading stress $\Sigma(r)$, acting on a given GB neighborhood at position r , and the external loading stress Σ , i.e., $\mathbf{f}(r) = \Sigma(r) - \Sigma$.

In addition, the rotational invariance of s suggests that Σ dependence in Eq. (E.2) can be expressed solely in terms of Σ invariants

$$\mathcal{F}(\Sigma) \rightarrow \mathcal{F}(\text{tr}(\Sigma), \det(\Sigma), \text{tr}(\Sigma_{\text{dev}}^2)). \quad (\text{E.3})$$

In the limit where the external loading is of hydrostatic form, $\Sigma = \Sigma_{\text{hyd}}$ (and $\Sigma_{\text{dev}} = 0$), a trivial solution is obtained with no stress fluctuations, $\mathbf{f} = 0$, implying that Σ_{dev} is the only relevant loading contribution in Eq. (E.3). To account for this limit, the following fluctuation stress tensor is finally proposed at position r ,

$$\mathbf{f}(r) = \eta(r) \mathbf{R}(r) \Sigma_{\text{dev}} \mathbf{R}(r)^T, \quad (\text{E.4})$$

where

$$\mathbf{R}(r) = \mathbf{R}(\alpha_1(r), \alpha_2(r), \alpha_3(r)) \quad (\text{E.5})$$

is a random rotation matrix with corresponding Euler angles $\alpha_j(r)$, and $\eta(r)$ is a random number with the assumed Gaussian distribution $\mathcal{N}(0, s^2(\eta))$ with $s(\eta) = \mathcal{F}(A^u, E_{12}, \dots)$.³³

In Eq. (E.4), the fluctuation stress tensor is modeled as the deviatoric part of the external loading³⁴ rescaled and rotated by a random amount to account for uncertainty of far-away grains that blur the external loading.

Using $\mathbf{f}(r)$ defined in Eq. (E.4) and a general expression $\sigma_{nn}^{(k)} = A^{(k)} \Sigma_{zz} + B^{(k)} (\Sigma_{xx} + \Sigma_{yy})$, the GB-normal-stress fluctuations evaluate to (using notation $f_{nn}^{(k)} = \Delta \sigma_{nn}^{(k)}$)

$$\begin{aligned} f_{nn}^{(k)}(r) &= A^{(k)} f_{zz}(r) + B^{(k)} (f_{xx}(r) + f_{yy}(r)) \\ &= (A^{(k)} - B^{(k)}) f_{zz}(r), \end{aligned} \quad (\text{E.6})$$

³³ For demonstrating purposes, a simple scalar multiplication η is used for rescaling, instead of a more general matrix multiplication.

³⁴ The hydrostatic part of the external loading is invariant to grain orientations and thus unable to produce strain incompatibility between the grains, which is the source of stress fluctuations.

where the $\text{tr}(\mathbf{f}(r)) = 0$ property of Eq. (E.4) has been used. The first two statistical moments follow as

$$\begin{aligned} \langle f_{nn}^{(k)}(r) \rangle_r &= (A^{(k)} - B^{(k)}) \int \eta \text{PDF}(\eta) d\eta \\ &\times \iiint \Sigma_{\text{dev},zz} \text{PDF}(\alpha_1, \alpha_2, \alpha_3) d\alpha_1 d\alpha_2 d\alpha_3 \\ &= 0, \end{aligned} \quad (\text{E.7})$$

and

$$\begin{aligned} s(f_{nn}^{(k)}(r)) &= \sqrt{\langle (f_{nn}^{(k)}(r))^2 \rangle_r} \\ &= |A^{(k)} - B^{(k)}| \sqrt{\int \eta^2 \text{PDF}(\eta) d\eta \iiint \Sigma_{\text{dev},zz}^2 \text{PDF}(\alpha_1, \alpha_2, \alpha_3) d\alpha_1 d\alpha_2 d\alpha_3} \\ &= \frac{2 \Sigma_{\text{mis}}}{3\sqrt{5}} |A^{(k)} - B^{(k)}| s(\eta), \end{aligned} \quad (\text{E.8})$$

with $\text{PDF}(\eta)$ corresponding to Gaussian distribution $\mathcal{N}(0, s^2(\eta))$ and $\text{PDF}(\alpha_1, \alpha_2, \alpha_3)$ to random orientation distribution. For crystal lattices with cubic symmetry, $|A^{(k)} - B^{(k)}|$ simplifies to $|3A^{(k)} - 1|/2$.

In overall, the derived expression for s suggests that the loading contribution to GB-normal-stress fluctuations can be trivially decoupled as

$$s(f_{nn}^{(k)}(r)) = \Sigma_{\text{mis}} \mathcal{F}(A^u, E_{12}, \dots). \quad (\text{E.9})$$

Appendix F. Macroscopic response of random grain boundaries

The upgraded models for local stresses $\tilde{\sigma}_{nn}^{(k)}$ and their macroscopic manifestation $\text{PDF}(\tilde{\sigma}_{nn}^{(k)})$ are typically used for GBs of a certain GB type, corresponding to fixed values of E_{12} and ν_{12} (together with δE_{12} and $\delta \nu_{12}$). The response of random GBs can therefore be estimated by integration over all GB types, hence taking into account all GBs in a given aggregate,

$$\text{PDF}_{\text{rnd}}(\tilde{\sigma}_{nn}^{(k)}) = \iint w(E_{12}, \nu_{12}) \text{PDF}(\tilde{\sigma}_{nn}^{(k)}) dE_{12} d\nu_{12}, \quad (\text{F.1})$$

where $w(E_{12}, \nu_{12})$ represents the distribution function of GB types in an aggregate and $\text{PDF}(\tilde{\sigma}_{nn}^{(k)})$ the macroscopic response of a specific GB type; cf. Eq. (38).

For aggregates with zero crystallographic texture, the response of random GBs can also be obtained more elegantly. There, the average σ_{nn} of all GBs with the same GB normal n (but arbitrary E_{12} and ν_{12}) should be equal to the external loading Σ , projected onto that GB plane, i.e., $\langle \sigma_{nn} \rangle = \sigma_{nn}^{(0)} = \Sigma_{zz}$. This is true because crystallographic orientations of grains are not correlated with orientations of GB planes, hence randomly distributed grain orientations are expected along every GB-normal direction n , providing an average (bulk) response. Thus,

$$\text{PDF}_{\text{rnd}}(\tilde{\sigma}_{nn}^{(k)}) \approx \text{PDF}(\tilde{\sigma}_{nn}^{(0)}), \quad (\text{F.2})$$

or, equivalently,

$$\text{PDF}_{\text{rnd}}(\tilde{\sigma}_{nn}^{(k)}) \approx \text{PDF}(\tilde{\sigma}_{nn}^{(k \geq 1)}) \Big|_{\substack{E_{12} + dE_{12} = 1 \\ E_3 + dE_3 = 1 \\ \nu_{12} + d\nu_{12} = \langle \nu \rangle}} \quad (\text{F.3})$$

In practice, the (approximate) PDF of stress response in a random aggregate can be obtained simply by convoluting the isotropic solution

$PDF(\sigma_{nn}^{(0)})$ with the Gaussian distribution $\mathcal{N}(0, s^2(f_{nn}))$, taking $s(f_{nn})$ from Eq. (39).

Appendix G. Grain-boundary-normal distribution in aggregates with elongated grains

In aggregates with zero morphological texture (i.e., with no preferred direction for grain shapes), the GB normals, $n = (\sin \theta \cos \psi, \sin \theta \sin \psi, \cos \theta)$, are uniformly distributed on a sphere, with corresponding distribution functions for the two angles

$$\begin{aligned} f(\cos \theta) &= \frac{1}{2}; & (-1 \leq \cos \theta \leq 1), \\ f(\psi) &= \frac{1}{2\pi}; & (0 \leq \psi \leq 2\pi). \end{aligned} \quad (G.1)$$

To generate an aggregate with grains elongated along the z-axis, a simple geometrical scaling can be applied to the initially isotropic aggregate

$$x \rightarrow x, \quad y \rightarrow y, \quad z \rightarrow \lambda_z z; \quad (\lambda_z > 0). \quad (G.2)$$

As a result of such transformation, the two distribution functions become

$$\begin{aligned} f(\cos \theta) &= \frac{\lambda_z}{2} \left(\frac{1}{1 + (\lambda_z^2 - 1) \cos^2 \theta} \right)^{3/2}; & (-1 \leq \cos \theta \leq 1), \\ f(\psi) &= \frac{1}{2\pi}; & (0 \leq \psi \leq 2\pi). \end{aligned} \quad (G.3)$$

The derived distributions are used to predict the stress response $PDF(\sigma_{nn}^{(k)})$ of any GB type within the elongated aggregate³⁵ (see Section 4).

References

Arafin, M., Szpunar, J., 2009. A new understanding of intergranular stress corrosion cracking resistance of pipeline steel through grain boundary character and crystallographic texture studies. *Corros. Sci.* 51, 119–128.

Benedetti, I., Aliabadi, M., 2013a. A three-dimensional cohesive-frictional grain-boundary micromechanical model for intergranular degradation and failure in polycrystalline materials. *Comput. Methods Appl. Mech. Engrg.* 265, 36–62.

Benedetti, I., Aliabadi, M., 2013b. A three-dimensional grain boundary formulation for microstructural modeling of polycrystalline materials. *Comput. Mater. Sci.* 67, 249–260.

Bower, A.F., 2010. *Applied Mechanics of Solids*. Taylor & Francis Group.

Burleigh, T., 1991. The postulated mechanisms for stress corrosion cracking of aluminum alloys: A review of the literature 1980–1989. *Corrosion* 47, 89–98.

Cox, B., 1970. Environmentally induced cracking of zirconium alloys. Technical report, Atomic Energy of Canada Limited.

Cox, B., 1990. Environmentally-induced cracking of zirconium alloys - A review. *J. Nuc. Mat.* 170, 1–23.

Diard, O., Leclercq, S., Rousselier, G., Cailletaud, G., 2002. Distribution of normal stress at grain boundaries in multicrystals: Application to an intergranular damage modeling. *Comput. Mater. Sci.* 25, 73–84.

Diard, O., Leclercq, S., Rousselier, G., Cailletaud, G., 2005. Evaluation of finite element based analysis of 3D multicrystalline aggregates plasticity. Application to crystal plasticity model identification and the study of strain fields near grain boundaries. *Int. J. Plast.* 21, 691–722.

El Shawish, S., Probabilistic two-scale modeling approach for predicting grain boundary fracture initiation and evolution in complex geometries, In preparation.

El Shawish, S., Hure, J., 2018. Intergranular normal stress distributions in untextured polycrystalline aggregates. *Eur. J. Mech. / A Solids* 72, 354–373.

El Shawish, S., Mede, T., Hure, J., 2021. A single grain boundary parameter to characterize normal stress fluctuations in materials with elastic cubic grains. *Eur. J. Mech. / A Solids* 89.

El Shawish, S., Vincent, P.G., Moulinec, H., Cizelj, L., Gélébart, L., 2020. Full-field polycrystal plasticity simulations of neutron-irradiated austenitic stainless steel: A comparison between FE and FFT-based approaches. *J. Nuc. Mat.* 529, 151927.

Fujii, T., Tohgo, K., Mori, Y., Miura, Y., Shimamura, Y., 2019. Crystallographic and mechanical investigation of intergranular stress corrosion crack initiation in austenitic stainless steel. *Mater. Sci. Eng. A* 751, 160–170.

³⁵ In aggregates with non-zero morphological texture the first two statistical moments do not scale anymore with $\text{tr}(\Sigma^{\text{lab}})$ and $\Sigma_{\text{mis}}^{\text{lab}}$, respectively.

Gonzalez, D., Simonovski, I., Withers, P., Quinta da Fonseca, J., 2014. Modelling the effect of elastic and plastic anisotropies on stresses at grain boundaries. *Int. J. Plast.* 61, 49–63.

Gupta, J., Hure, J., Tanguy, B., Laffont, L., Lafont, M., Andrieu, E., 2016. Evaluation of stress corrosion cracking of irradiated 304 stainless steel in PWR environment using heavy ion irradiation. *J. Nuc. Mat.* 476, 82–92.

Hershey, A., 1954. The elasticity of an isotropic aggregate of anisotropic cubic crystals. *J. Appl. Mech.* 21, 236–241.

Hure, J., El Shawish, S., Cizelj, L., Tanguy, B., 2016. Intergranular stress distributions in polycrystalline aggregates of irradiated stainless steel. *J. Nuc. Mat.*

IAEA, 2011. Stress corrosion cracking in light water reactors: Good practices and lessons learned. NP-T-3.13, IAEA Nuclear Energy Series.

Kanjarla, A., Van Houtte, P., Delannay, L., 2010. Assessment of plastic heterogeneity in grain interaction models using crystal plasticity finite element method. *Int. J. Plast.* 26, 1220–1233.

Koyama, M., Xi, Z.-J., Yoshida, Y., Yoshimura, N., Ushioda, K., Noguchi, H., 2015. Intergranular fatigue crack initiation and its associated small fatigue crack propagation in water-quenched Fe–C fully ferritic steel. *ISIJ Int.* 55 (11), 2463–2468.

Kröner, E., 1958. Berechnung der elastischen konstanten des vielkristalls aus den konstanten des einkristalls. *Z. Physik* 151, 504.

Le Millier, M., Calonne, O., Crépin, J., Duhamel, C., Fournier, L., Gaslain, F., Héripré, E., Toader, O., Vidalenc, Y., Was, G., 2013. Influence of strain localization on IASCC of proton irradiated 304L stainless steel in simulated PWR primary water. In: 16th International Conference on Environmental Degradation of Materials in Nuclear Power Systems - Water Reactors.

Lebensohn, R., Kanjarla, A., Eisenlohr, P., 2012. An elasto-viscoplastic formulation based on fast Fourier transforms for the prediction of micromechanical fields in polycrystalline materials. *Int. J. Plast.* 32–33, 59–69.

Liang, D., Hure, J., Courcelle, A., El Shawish, S., Tanguy, B., 2021. A micromechanical analysis of intergranular stress corrosion cracking of an irradiated austenitic stainless steel. *Acta Mater.* 204, 116482.

Liu, T., Xia, S., Bai, Q., Zhou, B., Lu, Y., Shoji, T., 2019. Evaluation of grain boundary network and improvement of intergranular cracking resistance in 316L stainless steel after grain boundary engineering. *Materials* 12, 242–258.

Nishioka, H., Fukuya, K., Fujii, K., Torimaru, T., 2008. IASCC initiation in highly irradiated stainless steels under uniaxial constant load conditions. *J. Nuc. Sci. and Tech.* 45, 1072–1077.

Panter, J., Viguier, B., Cloué, J., Foucault, M., Combrade, P., Andrieu, E., 2006. Influence of oxide films on primary water stress corrosion cracking initiation of alloy 600. *J. Nuc. Mat.* 348, 213–221.

Quey, R., Dawson, P.R., Barbe, F., 2011. Large-scale 3D random polycrystals for the finite element method: Generation, meshing and remeshing. *Comput. Methods Appl. Mech. Engrg.* 200, 1729–1745.

Rahimi, S., Engelberg, D.L., Duff, J.A., Marrow, T.J., 2009. In situ observation of intergranular crack nucleation in a grain boundary controlled austenitic stainless steel. *J. Microsc.* 233 (3), 423–431.

Rahimi, S., Marrow, T.J., 2011. Effects of orientation, stress and exposure time on short intergranular stress corrosion crack behaviour in sensitised type 304 austenitic stainless steel. *Fatigue Fract. Eng. Mater. Struct.* 35, 359–373.

Ranganathan, S.I., Ostaja-Starzewski, M., 2008. Universal elastic anisotropy index. *Phys. Rev. Lett.* 101, 055504.

Sfantos, G., Aliabadi, M., 2007. Multi-scale boundary element modelling of material degradation and fracture. *Comput. Methods Appl. Mech. Engrg.* 196, 1310–1329.

Shen, C., Shewmon, P., 1990. A mechanism for hydrogen-induced intergranular stress corrosion cracking in alloy 600. *Metall. Trans. A* 21A, 1261–1271.

Simmons, G., Wang, H., 1971. *Single Crystal Elastic Constants and Calculated Aggregate Properties. A Handbook*. The MIT Press.

Simulia, 2016. ABAQUS 6.14-2.

Speidel, M., 1975. Stress corrosion cracking of aluminum alloys. *Metall. Mater. Trans. A* 6A, 631–651.

Stephenson, K., Was, G., 2014. Crack initiation behavior of neutron irradiated model and commercial stainless steels in high temperature water. *J. Nuc. Mat.* 444, 331–341.

Stratulat, A., Duff, J.A., Marrow, T.J., 2014. Grain boundary structure and intergranular stress corrosion crack initiation in high temperature water of a thermally sensitised austenitic stainless steel, observed in situ. *Corros. Sci.* 85, 428–435.

Van Rooyen, D., 1975. Review of the stress corrosion cracking of inconel 600. *Corrosion* 31, 327–337.

Wang, Z., Atrens, A., 1996. Initiation of stress corrosion cracking for pipeline steels in a carbonate-bicarbonate solution. *Metall. Mater. Trans. A* 27A, 2686–2691.

West, E.A., Was, G.S., 2011. A model for the normal stress dependence of intergranular cracking of irradiated 316L stainless steel in supercritical water. *J. Nuc. Mat.* 408 (2), 142–152.

Zener, C., 1948. *Elasticity and Anelasticity of Metals*. University of Chicago.

Zhang, Z., Xia, S., Bai, Q., Liu, T., Li, H., Zhou, B., Wang, L., Ma, W., 2019. Effects of 3D grain boundary geometrical angles and the net normal stress on intergranular stress corrosion cracking initiation in a 316 stainless steel. *Mater. Sci. Eng. A* 765, 138277.